Morphodynamic modeling of an embayed beach under wave group forcing

A. J. H. M. Reniers

Faculty of Civil Engineering and Geosciences, Delft University of Technology, Delft, Netherlands

J. A. Roelvink[1]

WL|Delft Hydraulics, Delft, Netherlands

E. B. Thornton

Oceanography Department, Naval Postgraduate School, Monterey, California, USA

[1] The morphodynamic response of the nearshore zone of an embayed beach induced by wave groups is examined with a numerical model. The model utilizes the nonlinear shallow water equations to phase resolve the mean and infragravity motions in combination with an advection-diffusion equation for the sediment transport. The sediment transport associated with the short-wave asymmetry is accounted for by means of a time-integrated contribution of the wave nonlinearity using stream function theory. The two-dimensional (2-D) computations consider wave group energy made up of directionally spread, short waves with a zero mean approach angle with respect to the shore normal, incident on an initially alongshore uniform barred beach. Prior to the 2-D computations, the model is calibrated with prototype flume measurements of waves, currents, and bed level changes during erosive and accretive conditions. The most prominent feature of the 2-D model computations is the development of an alongshore quasi-periodic bathymetry of shoals cut by rip channels. Without directional spreading, the smallest alongshore separation of the rip channels is obtained, and the beach response is self-organizing in nature. Introducing a small amount of directional spreading (less than 2°) results in a strong increase in the alongshore length scales as the beach response changes from self-organizing to being quasi-forced. A further increase in directional spreading leads again to smaller length scales. The hypothesized correlation between the observed rip spacing and wave group forced edge waves over the initially alongshore uniform bathymetry is not found. However, there is a correlation between the alongshore length scales of the wave group-induced quasi-steady flow circulations and the eventual alongshore spacing of the rip channels. This suggests that the scouring associated with the quasi-steady flow induced by the initial wave groups triggers the development of rip channels via a positive feedback mechanism in which the small scour holes start attracting more and more discharge. *INDEX TERMS:* 4255 Oceanography: General: Numerical modeling; 4512 Oceanography: Physical: Currents; 4546 Oceanography: Physical: Nearshore processes; 4558 Oceanography: Physical: Sediment transport; *KEYWORDS:* rip currents, rip channel spacing, morphodynamic coupling, sediment transport, edge and infragravity waves, directional spreading of incident waves

1. Introduction

[2] Rhythmic patterns in bathymetry are frequently observed in the nearshore. Beach cusps are a well known example and exist on many beaches [e.g., *Komar*, 1976].

Large crescentic bars were reported by *Clos-Arceduc* [1962] on the Mediterranean coastline of Algiers. More complex patterns have been reported by *Hom-ma and Sonu* [1963], looking at the rhythmicity of longshore bars on the Japanese coasts. *Wright and Short* [1984] examined the nearshore variability on Australian beaches and introduced a classification of the various beach states observed. This classification was extended by *Lippmann and Holman* [1990], who examined the day-to-day variability of the nearshore morphology at Duck, North Carolina, utilizing video

---

[1]Also at Faculty of Civil Engineering and Geosciences, Delft University, Delft, Netherlands.

techniques. Using similar techniques, *Ranasinghe et al.* [1999] describe the behavior of irregularly spaced rip channels on the embayed beach of Palm Beach, Australia. The spatial variability of the nearshore bars along the Dutch coast was examined by *Wijnberg and Terwindt* [1995] on the basis of the JARKUS profile data set (approximately three decades of annual cross-shore profiles at approximately 250-m intervals along 120 km of the Dutch coast). *Van Enckevort and Ruessink* [2001] utilized video observations to examine the daily to yearly variability of the nearshore bar behavior at Noordwijk aan Zee, the Netherlands. All of these observations show that the behavior of the nearshore bathymetry is rather complex and that there is a need to increase our understanding of the underlying mechanisms.

[3] Different explanations have been suggested for the observed rhythmic morphodynamic response. One class of explanations is based on (in-)stability models that consider an initial equilibrium state which is subject to small perturbations in the forcing and/or water depth. Morphodynamic instabilities occur through the coupling of the sediment transport and hydrodynamic conditions (waves and currents), generally growing exponentially in time. The first instability model of the nearshore bathymetry was done by *Barcilon and Lau* [1973] extending the work of *Kennedy* [1963], to examine the generation and spacing of transverse bars induced by an uniform longshore (tidal) current over a mildly sloping beach. *Hino* [1974] included the effects of waves to drive a current, obtaining solutions which correspond to a rip channel system for normally incident waves to oblique bars for obliquely incident waves. Lately this approach has received increased attention with the work of *Christensen et al.* [1994], *Falques et al.* [1996, 2000], *Deigaard et al.* [1999], and *Ribas et al.* [2003], with more sophisticated descriptions of the sediment transport taking into account the stirring by the short waves. In general, these linear stability models predict length scales and bar orientations comparable to field observations. *Caballeria et al.* [2002] included the nonlinear terms in their model to predict the morphological evolution of an initially equilibrated planar sloping beach subject to normally incident regular waves on which small topographic perturbations were superimposed, and found the generation of either transverse or crescentic bars depending on offshore wave height and sediment characteristics. *Damgaard et al.* [2002] compared their nonlinear model results with results from a linear stability analysis for random (JONSWAP) waves normally incident on a barred beach and obtained good correspondence for both the alongshore rip spacing and initial growth rates.

[4] A second class of models is based on the residual flow patterns associated with infragravity waves and more specifically edge waves. Typical wave periods associated with the infragravity waves are in the order of 20 seconds to minutes. The spatial scales associated with the infragravity waves can be of the same order as the observed patterns present in the bathymetry $O(50)$ m and larger, hence their potential importance for the nearshore morphology. *Bowen and Inman* [1969] considered a combination of standing edge waves with incident waves of the same frequency to explain the generation of a rip current system. Using different combinations of phase locked edge waves, *Holman and Bowen* [1982] obtained a large set of solutions

that lead to complex bar patterns. More recently *Symonds and Ranasinghe* [2000] extended the approach of *Bowen and Inman* [1969] to the case of edge waves interacting with incident wave groups, thus increasing the alongshore spacing of the rip channels. The important difference between the two classes of models is that in the first case the morphodynamic response is self organizing in nature whereas in the second case it is forced.

[5] Here we adopt a process based approach, modeling the various processes at the scale of the wave group motions, with the aim to predict the changes that will occur in the nearshore bathymetry with changes in the short-wave forcing. Note that this approach does not prohibit developments associated with self organizing processes. Attention is focused on an embayed beach, which limits the computational domain and simplifies the lateral boundary conditions, but still allows for complex (quasi-)rhythmic features such as observed by *Ranasinghe et al.* [1999]. Prior to the more complex 2-D computations, the morphodynamic model is verified with measurements obtained during the LIP11D test in the Delta Flume [*Arcilla et al.*, 1994]. These experiments considered both erosive (test 1B) and accretive (test 1C) hydrodynamic conditions, reflecting storm and post storm conditions.

[6] The primary objective of the present study is to assess the effects of wave group forcing on the nearshore morphodynamic response with specific attention to infragravity waves. The starting point is an alongshore uniform, single barred beach, assumed to be the result of a storm during which the nearshore bathymetry transformed from complex three-dimensional (3-D) to alongshore uniform (2-D) as is frequently observed [*Lippmann and Holman*, 1990; *Ranasinghe et al.*, 1999]. Next, accretive, post storm wave conditions are applied to which the initial bathymetry is not equilibrated, which in principle precludes the use of a linear stability analysis. Note that in cases where alongshore features develop on a significantly shorter time scale than the cross-shore profile evolution a linear stability analysis can still be applied. To test the hypothesis that the quasi-periodic beach response results from the presence of edge waves, computations on a fixed alongshore uniform bed are performed prior to the morphodynamic computations to relate observed preferential alongshore length scales in the wave group-induced motions to the eventual complex beach geometry. Effects resulting from changes in wave energy, peak period, initial beach profile, etc. are outside the scope of the present study and have therefore not been taken into account. The present study is an extension of the work by *Reniers et al.* [2000], who considered the morphodynamic response of an initially plane sloping embayed beach under wave group forcing.

2. Model Description
2.1. Introduction

[7] The numerical model is a research version of Delft3D (www.wldelft.nl). New wave and roller modules describing wave propagation and breaking, operating on the timescale of wave groups, are coupled to a depth averaged nonlinear flow model to predict the time-dependent infragravity flow field. The model concept is illustrated in Figure 1, showing the propagation of grouped short waves of which only the
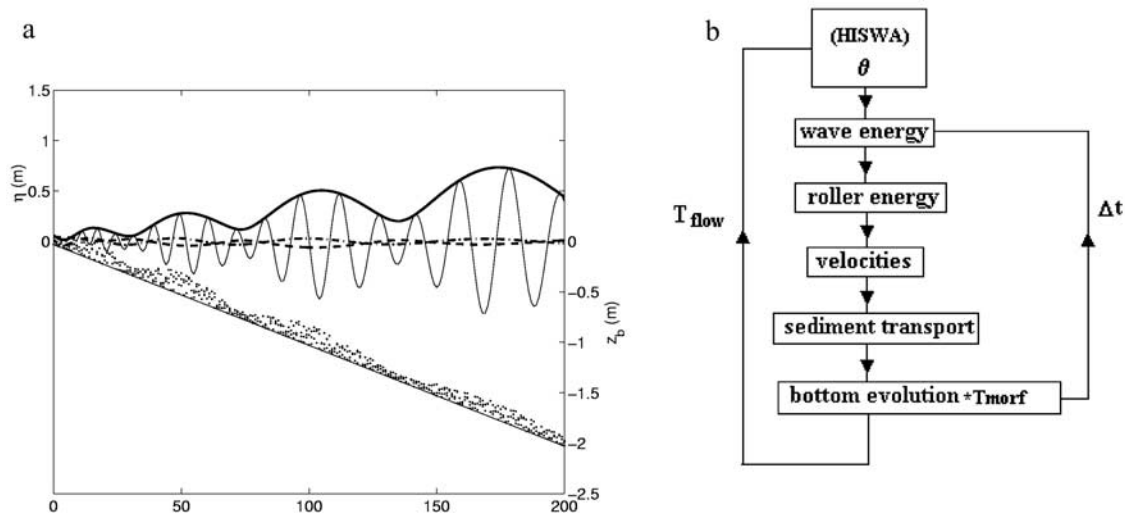
Figure 1. (a) Depiction of wave groups normally incident on a beach with corresponding wave envelope (thick solid line), bound infragravtiy wave (dashed line), and free returning infragravity wave (dash-dotted line). (b) Flow diagram for morphodynamic computations.

wave energy on the group scale, proportional to the square of the wave envelope, is modeled. Under the groups of short high waves, water is forced toward the areas with smaller waves, thus creating a bound infragravity wave, that is $180°$ out of phase with the short-wave groups, traveling with the group velocity. Within the surf zone, the wave group modulation is destroyed by wave breaking, and consequently the bound infragravity wave is released, reflects off the beach, and returns as a free wave. In the case of small incidence wave angles, the free infragravity wave is able to escape (or leak) to deeper water. However, for increased angles of incidence, the free infragravity waves may become refractively trapped to the nearshore [*Schäffer*, 1994; *Herbers et al.*, 1995].

[8] The wave driver input is obtained from a frequency direction energy density wave spectrum, $E(f, \theta)$. The model considers the wave energy associated with wave groups, made up of the directionally spread spectral components, to generate infragravity waves through triad interactions (described below). The energy associated with the wave groups is propagated shoreward, where the mean wave direction is obtained from the precomputed wave refraction (Figure 1b) utilizing the wave model HISWA [*Holthuijsen et al.*, 1989]. Wave energy released at wave breaking is first transferred to roller energy prior to dissipation causing a spatial lag between the location of wave breaking and the actual dissipation. Diffraction and wave current interaction are neglected at present.

[9] The temporal and spatial variation (on the wave group scale) of the wave and roller energy is used to calculate the radiation stresses. The mean and wave group motions are solved using nonlinear shallow water equations forced by radiation stresses to phase resolve bound and free infragravity waves, both trapped (edge waves) and leaky. In addition to the mean and infragravity motions, the time variation allows for the generation of shear instabilities in strongly sheared currents. The flow model uses eddy viscosity to describe turbulent momentum mixing. The nonlinear bottom shear stress considers wave-current interaction.

[10] The model calculates the phase resolved infragravity sediment transport with an advection-diffusion model. The sediment transport module includes transport by the mean currents and short and infragravity waves. Sediment is predominantly stirred by the wave orbital motion and wave breaking-induced turbulence. The skewness of the short waves, responsible for onshore sediment transport and the onshore migration of bars, is parameterized on the timescale of the infragravity waves using a nonlinear Fourier representation.

[11] The divergence of sediment transport results in temporal changes of the nearshore morphology. These changes in water depth feed back to affect the wave energy propagation and thereby the mean and infragravity velocities and sediment concentration and so on. Computations are carried out for a duration T_{flow}, after which the mean incidence angle is recomputed with HISWA, where T_{flow} is assumed to be small with respect to the morphological timescale (Figure 1b). The morphological response thus can exhibit both forced behavior (at the scales of the infragravity waves) and free behavior owing to the local nonlinear feedback between flow and morphology and therefore encompasses both of the previously mentioned rip channel generation mechanisms.

[12] It is essential to phase resolve the infragravity waves as the phase relationship between the short waves (which act to stir the sediments into suspension) and the infragravity waves depends on the mix of free and bound infragravity energy. For example, the bound infragravity waves are $180°$ out of phase with the short-wave groups traveling with the group velocity. The orbital motion of the short waves stirs up the sediment, which is then transported by the infragravity velocity. Given that groups of high waves that stir up more sediment coincide with the troughs of the infragravity waves (Figure 1a), the predominant transport direction will be offshore. Only close to the shoreline is this direction reversed as the infragravity waves modulate the depth-limited short-wave breaking resulting in higher groups of short waves propagating on top of the infragravity wave crests.

[13] In the following, a summary of the wave, flow and sediment transport equations is presented. The research version of the wave and flow model has been successfully compared with both mean rip current measurements obtained during the RDEX field experiment at Palm Beach Australia [*Reniers et al.*, 2001] and infragravity motions measured during the RIPEX field experiment in Monterey bay, USA [*Reniers et al.*, 2002a].

2.2. Wave Equations

[14] Motions on the timescale of wave groups are considered in the following. To that end all quantities have been averaged over the timescale of the incident wave period. The incident short-wave spectrum is assumed to be narrow in both frequency and direction. The balance for the short-wave energy, E_w, describing the propagation of the obliquely incident short-wave groups on a variable bathymetry is then given by:

$$\frac{\partial E_w}{\partial t} + \frac{\partial E_w c_g \cos(\theta)}{\partial x} + \frac{\partial E_w c_g \sin(\theta)}{\partial y} = -D_w \quad (1)$$

where c_g represents the group velocity associated with the peak period of the waves, D_w the wave energy dissipation, x the distance in the cross-shore (positive onshore), y the distance alongshore (following the cartesian convention) and θ the mean wave incidence angle with respect to the x axis. The spatially and temporally varying wave energy is defined along the upwave boundary. To model the wave energy dissipation due to wave breaking the dissipation formulation of *Roelvink* [1993a] is used:

$$D_w = 2\alpha f_p E_w \left[1 - exp\left[-\left(\frac{E_w}{\gamma^2 E_{ref}} \right)^{\frac{n_d}{2}} \right] \right] \quad (2)$$

with:

$$E_{ref} = \frac{1}{8}\rho g h^2 \quad (3)$$

where f_p is the peak frequency, γ is a wave breaking parameter representing saturation, α a coefficient of $O(1)$, n_d a dissipation parameter corresponding to the randomness of the incident waves, ρ is the water density, g the gravitational acceleration and h represents the total water depth (including setup and infragravity surface elevation). The wave energy dissipation serves as input in the balance for the kinetic roller energy, E_r [*Nairn et al.*, 1990; *Stive and de Vriend*, 1994]:

$$\frac{\partial E_r}{\partial t} + \frac{\partial 2E_r c \cos(\theta)}{\partial x} + \frac{\partial 2E_r c \sin(\theta)}{\partial y} = -D_r + D_w \quad (4)$$

where c is the phase velocity and D_r represents the roller energy dissipation expressed by:

$$D_r = \frac{2g \sin(\beta)E_r}{c} \quad (5)$$

Choosing β, the single unknown in equation (4), E_r, is solved for, which is taken to be zero at the up-wave boundary.

2.3. Flow Equations

[15] The short-wave averaged, depth-averaged velocity field is computed with nonlinear shallow water equations. The wave group varying velocities, u and v in the x and y direction respectively, include the wave-induced drift velocity [*Stokes*, 1847]:

$$u = u^E + u^S \quad (6)$$

where the superscripts E and S stand for Eulerian and Stokes, respectively, and a similar expression is used for the v component. This allows differentiating between the onshore velocity near the surface owing the waves and flow beneath that can include the offshore undertow. Separating the velocities in this manner can be important in specifying the mass flux and the bottom shear stress. The continuity equation is given by

$$\frac{\partial \eta}{\partial t} + \frac{\partial(hu)}{\partial x} + \frac{\partial(hv)}{\partial y} = 0 \quad (7)$$

where η represents the mean and infragravity surface elevation. The cross-shore momentum balance is given by

$$\frac{\partial u}{\partial t} + u\frac{\partial u}{\partial x} + v\frac{\partial u}{\partial y} = -F_x - g\frac{\partial \eta}{\partial x} + \nu_t\left(\frac{\partial^2 u}{\partial x^2} + \frac{\partial^2 u}{\partial y^2}\right) - \frac{\tau_x}{h} \quad (8)$$

where the first term of the RHS represents the wave-induced forcing, the second term the cross-shore pressure gradient, the third term the turbulent lateral mixing and τ_x represents the combined short-wave and (Eulerian) current bottom shear stress [*Soulsby et al.*, 1993] operating in the cross-shore direction. The alongshore momentum equation is given by

$$\frac{\partial v}{\partial t} + u\frac{\partial v}{\partial x} + v\frac{\partial v}{\partial y} = -F_y - g\frac{\partial \eta}{\partial y} + \nu_t\left(\frac{\partial^2 v}{\partial x^2} + \frac{\partial^2 v}{\partial y^2}\right) - \frac{\tau_y}{h} \quad (9)$$

where τ_y represents the combined short-wave and current bottom shear stress in the alongshore direction. The wave- and roller-induced forces F_x and F_y are defined as

$$F_x = \frac{1}{\rho h}\left(\frac{\partial S_{xx}}{\partial x} + \frac{\partial S_{yx}}{\partial y}\right) \quad (10)$$

$$F_y = \frac{1}{\rho h}\left(\frac{\partial S_{yy}}{\partial y} + \frac{\partial S_{xy}}{\partial x}\right) \quad (11)$$

where the subscripts refer to the direction in which the forces act and the radiation stress tensor, S_{ij}, is obtained from linear wave theory including the roller contribution [*Reniers et al.*, 2002b].

[16] The turbulent eddy viscosity, ν_t, associated with lateral mixing is assumed to be related to wave breaking ([*Battjes*, 1975]:

$$\nu_t = h\left(\frac{D_r}{\rho}\right)^{\frac{1}{3}} \quad (12)$$

where the roller energy dissipation, D_r, is obtained from the wave transformation equation (4). The friction coefficient used in the bed shear stress formulation is kept constant and is based on the successful comparisons with both mean flow conditions [*Reniers et al.*, 2001] and infragravity conditions [*Reniers et al.*, 2002a, submitted manuscript, 2002].

2.4. Sediment Transport and Bottom Changes

[17] The sediment transport is modeled with a depth averaged, advection diffusion equation [*Galappatti*, 1983]:

$$\frac{\partial}{\partial t}hC + \frac{\partial}{\partial x}hCu^E + \frac{\partial}{\partial y}hCv^E = \frac{hC_{eq} - hC}{T_s} \qquad (13)$$

where C represents the wave group varying, depth averaged, sediment concentration. The diffusion of the sediment is represented by an adaptation time T_s, given by a simple approximation based on the local water depth, h, and sediment fall velocity w_s:

$$T_s = 0.05\frac{h}{w_s} \qquad (14)$$

The equilibrium concentration, C_{eq}, representing the source term in equation (13), is obtained from the sediment transport formulation of Soulsby-van Rijn [*Soulsby*, 1997]:

$$
\begin{aligned}
C_{eq} = &\frac{\rho(A_{sb} + A_{ss})}{h} \\
&\cdot \left(\left((\bar{u}^E + \bar{v}^E)^2 + \frac{0.018u_{rms}^2}{C_d} \right)^{\frac{1}{2}} - u_{cr} \right)^{2.4} (1 - 3.5m)
\end{aligned} \qquad (15)
$$

where sediment is stirred by the 10-min mean (denoted by the overbar) Eulerian velocity, and the combined near bed, short-wave velocity, and wave breaking-induced turbulence motion, u_{rms}, given by:

$$u_{rms} = \sqrt{u_{rms,hi}^2 + 0.5k_b} \qquad (16)$$

where the root mean square near bed, short-wave orbital velocity amplitude, $u_{rms,hi}$, is obtained using the wave group varying wave energy applying linear wave theory, and the near bed, wave breaking-induced turbulence, k_b, is given by [*Roelvink and Stive*, 1989]:

$$k_b = \frac{\left(\frac{D_r}{\rho}\right)^{\frac{2}{3}}}{exp\left(\frac{h}{H_{rms,hi}}\right) - 1} \qquad (17)$$

where the short-wave root mean square wave height $H_{rms,hi}$ is again obtained from the wave energy balance using linear wave theory. The combined mean and orbital velocity have to exceed a threshold value, u_{cr}, before sediment is set in motion. The drag coefficient, C_d, is due to mean current alone and m represents the local bed-slope. The bed load coefficients A_{sb} and the suspended load coefficient A_{ss} are functions of the sediment grain size, relative density of the sediment and the local water depth (see *Soulsby* [1997] for details).

[18] The additional stirring of sediment by the infragravity motions is not explicitly taken into account in the present sediment transport formulation, but instead is assumed to be implicit in the near-bed orbital motion. To include the infragravity velocities in the sediment stirring requires a recalibration of the coefficients A_{sb} and A_{ss}, which are presently based on a comparisons with measurements ignoring the explicit infragravity wave contribution in the stirring [*van Rijn*, 1993].

[19] To solve for the transport velocities, u^E and v^E, the Stokes drift has to be subtracted from the computed velocities, u and v, where the Stokes drift is defined as [*Phillips*, 1977]:

$$u^S = \frac{M_x}{\rho h} \qquad (18)$$

with the inclusion of the roller contribution in the mass flux:

$$M_x = \frac{(E_w + 2E_r)\cos(\theta)}{c} \qquad (19)$$

and a similar expression for the alongshore component.

[20] To be able to model the morphodynamic behavior of a coastline, the sediment transport associated with the asymmetry of the nonlinear short waves also has to be taken into account. Under the short-wave crest, the orbital velocity is relatively high, stirring up sediment and transporting it in the onshore direction. Under the trough the orbital velocity is smaller, thus transporting less sediment in the offshore direction. The net effect is typically an onshore transport of sediment. In reality the effect is considerably more complicated than sketched here, where the phase lags between the sediment concentration and the near-bed orbital velocity determine the magnitude and even the direction of the transport [*Ribberink and Chen*, 1993; *Janssen et al.*, 1998]. To retain the time and spatial scales inherent of the wave group motions, this transport has been averaged over the peak wave period, T_p [*Reniers et al.*, 2000]:

$$\tilde{u} = \alpha_w \frac{\int_0^{T_p} C'_{eq}(t)u'_b(t)dt}{\int_0^{T_p} C'_{eq}(t)dt} \qquad (20)$$

where u'_b is the instantaneous near bed velocity and C'_{eq} the equilibrium sediment concentration and the prime denotes intrawave variables. The calibration factor α_w is obtained from comparisons with measurements. The nonlinear, near bed velocities are computed from the wave energy, (equation (1)), with stream function theory [*Rienecker and Fenton*, 1981]. The wave asymmetry related velocity $\tilde{u}$, is added to the instantaneous Eulerian velocity u^E, which both vary on the wave group scale.

[21] Finally the bottom changes are obtained from continuity:

$$\frac{\partial z_b}{\partial t} = \frac{-1}{\rho_s(1 - n_p)} \frac{hC_{eq} - hC}{T_s} T_{morf} \qquad (21)$$

Table 1. Root Mean Square Short-Wave Height, Peak Period, and Sediment Fall Velocity for Tests 1B and 1C During the LIP11D Experiment

Parameter	$H_{rms,hi}$, m	T_p, s	w_s, m/s
Test 1B	1.0	5.0	0.014
Test 1C	0.4	8.0	0.014

where n_p represents the porosity, ρ_s the sediment density and T_{morf} a morphological time step to speed up the morphological evolution (Figure 1b).

3. One-Dimensional Morphodynamic Verification

[22] Prior to the more complex 2-D computations, the model is calibrated with prototype measurements obtained in the Delta flume during the LIP11D experiment [*Arcilla et al.*, 1994]. The measurements considered both erosive and accretive wave conditions (Table 1). The erosive condition, test 1B, was run for 18 hours, with bottom profile measurements at hourly intervals to monitor the morphological changes.

[23] The bottom profile 7 hours into test 1B is used to compare the hydrodynamic model output with the measurements (Figures 2a and 2b). The wave energy at the offshore model boundary was obtained by applying a Hilbert trans-

form on the measured surface elevation (at 20 m from the paddle) with a low-frequency cut off at half the peak frequency, corresponding to wave group motions only. The root mean square low-frequency wave height, $H_{rms,lo}$, is defined as $2\sqrt{2}$ times the standard deviation of the low-frequency surface elevation (and $H_{rms,hi}$ as its high-frequency equivalent). The root mean square low-frequency velocities, $U_{rms,lo}$ and $V_{rms,lo}$, are defined as the standard deviation of the cross-shore and alongshore low-frequency velocities respectively. The wave transformation was optimized by calibrating the wave dissipation coefficient γ (see Table 2).

[24] The computed and measured wave transformations compare well (Figure 2a) for $\gamma = 0.50$, with more intense wave breaking occurring over the bar, little wave dissipation in the trough, followed by additional wave breaking at the shore line. The roller dissipation coefficient β was set at 0.1. The computed mean velocities, forced by the wave and roller dissipation, are compared with measured mean depth-integrated velocities based on five velocity points in the vertical [*Arcilla et al.*, 1994]. There is a significant mismatch within the bar trough area (Figure 2b), with a spatial lag between the computed and measured maximum return flow velocities. It is evident that the resulting profile behavior will be different from the observations if the presently computed velocities are used to drive the sediment transport. To account for the
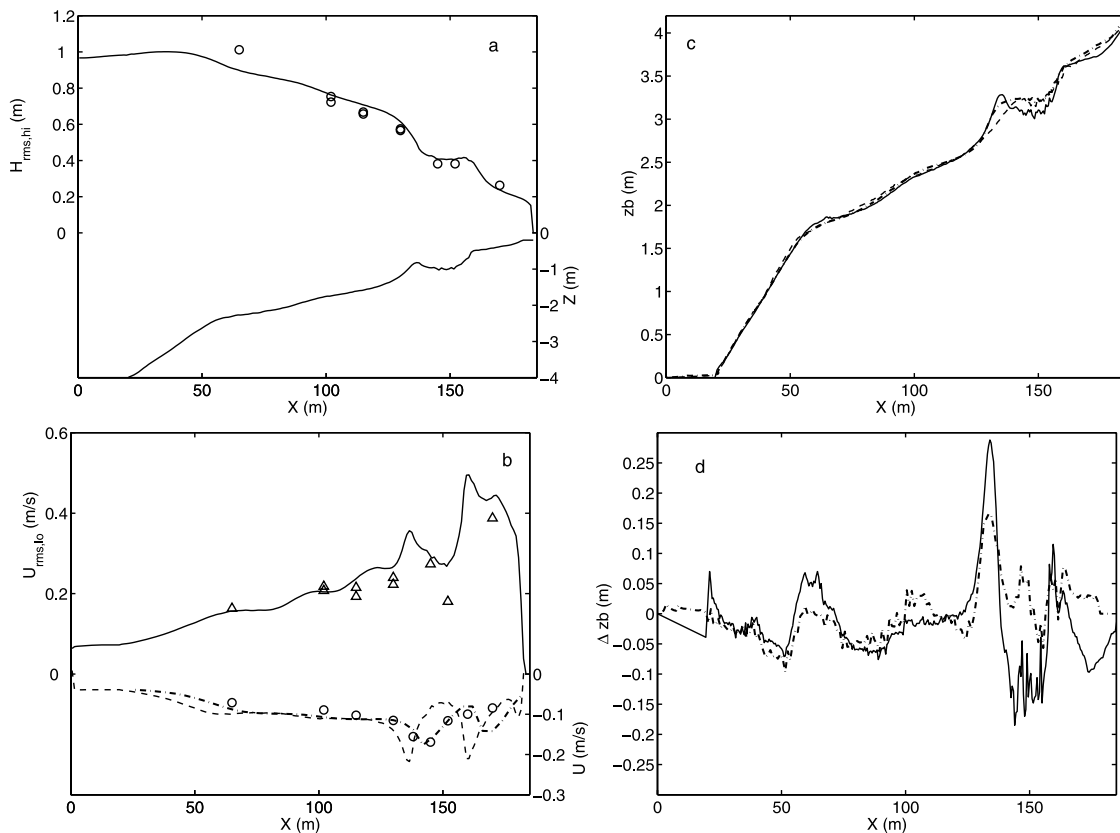

Figure 2. Test 1B. (a) Computed (solid line) and measured (circles) $H_{rms,hi}$. Bottom profile given as a reference. (b) Computed (solid line) and measured (triangles) $U_{rms,lo}$ and mean flow with (dash-dotted line) and without (dashed line) breaker delay compared to measurements (circles). (c) Initial (dashed line), measured (solid line), and computed (dash-dotted) bottom profiles after 18 hours. (d) Computed (dash-dotted) and measured (solid) bed level changes after 18 hours.

Table 2. Parameter Settings for 1-D Morphodynamic Computations

Parameter	α	γ	β	n_d	α_w	T_{flow}, min	T_{morf}
Test 1B	1.0	0.50	0.1	20	0.75	15	8
Test 1C	1.0	0.40	0.1	20	0.75	15	8

fact that short waves require some time to react to the local changes in the bathymetry, a triangular weighting function is introduced [*Roelvink et al.*, 1995] in the computation of the mean Stokes drift:

$$\tilde{u}^S(x) = \frac{\int_{x-L}^{x} (L - (x - \xi))\bar{u}^S(\xi)d\xi}{\int_{x-L}^{x} (L - (x - \xi))d\xi} \qquad (22)$$

where L is the wavelength at the peak frequency. This improves the comparison considerably, both quantitatively and qualitatively, where maximum computed and measured return flows now occur at the same location (Figure 2b). The largest mismatch is at the most shoreward point which is likely associated with the limited water depth at this location resulting in infrequent inundation of the (higher) current meters. To obtain the total Stokes drift, u^S, which is used to compute the total Eulerian velocities, the mean contribution in equation (18) is replaced with the weighted mean Stokes drift, $\tilde{u}^S$, obtained from equation (22).

[25] The wave paddle in the Delta Flume was operated with active wave absorption [*Klopman*, 1995] to prevent rereflections of infragravity waves. In the modeling, this is simulated by applying a Riemann boundary condition that allows for the radiation of the outgoing infragravity waves [*Verboom and Slob*, 1984]. Neither the modeling nor the wave paddle steering takes account of the presence of a bound infragravity wave at the paddle, thus generating a small spurious long wave that travels ahead of the bound infragravity wave [*Roelvink*, 1993b]. At the shoreline, a zero flux boundary condition is applied at a minimal water depth of 0.2 m. Intermittent drying and flooding is accounted for [*Stelling*, 1984]. Both computed and measured $U_{rms,lo}$ increase strongly with decreasing depth, with a good match offshore (Figure 2b). At the bar crest, the computed $U_{rms,lo}$ has a local maximum, which is not resolved by the measurements. Inshore of the trough, the computations overestimate the measured $U_{rms,lo}$ by approximately 20%.

[26] The profile evolution is considered next (Figures 2c and 2d). Starting with the initial measured profile, the morphological changes are computed for a duration of 18 hours. The corresponding input parameters are given in Table 1. The measured profile response to the erosive conditions present during test 1B, i.e., increasing bar amplitude while moving offshore, is reproduced by the model computations (Figure 2c). The differences between the final computed and measured profiles are mostly associated with the shape of the bar, which is more sharp crested in the measurements. Still, the computed and measured changes compare reasonably well both qualitatively (spatial distribution) and quantitatively (Figure 2d).

[27] A similar assessment for the accretive conditions is performed with test 1C, which was run for 14 hours. Computed and measured wave transformation compare well for a γ of 0.4 (Figure 3a). The corresponding mean return flow compares reasonably well with the measurements (Figure 3b) provided the spatial delay, equation (22), is taken into account. Both computed and measured infragravity velocities increase with decreasing depth, with a clear local maximum located near the bar crest, which is now resolved by the measurements, and a second maximum near the shore line (Figure 3b). For the accretive conditions during test 1C, the bar increases in amplitude while moving onshore (Figure 3c). The computations do show an increase in amplitude of the bar crest, but the onshore motion is only partially reproduced. There is reasonable qualitative and quantitative agreement also further offshore where both computed and measured bed level changes are small (Figure 3d).

[28] The comparisons for both erosive and accretive conditions in a 1-D setting show that the general morphodynamic response is reflected in the present computations. Wave transformation and the corresponding mean and infragravity motions are well predicted throughout the surf zone. Bar growth occurs under both erosive and accretive conditions. The offshore migration of the bar crest during erosive conditions is mostly reproduced, which is not the case for the onshore migration during the accretive conditions. Differences occur mostly in bar shape and the profile response close to the shoreline. Part of these observed differences can be attributed to the fact that the vertical dimension in both the computed flow and sediment concentration is not resolved at present.

4. Two-Dimensional Morphodynamic Computations

4.1. Introduction

[29] Two-dimensional computations are performed to assess the influence of wave group forcing on the nearshore morphological response with specific attention on infragravity waves. A number of cases with different directional spreading are considered as given in Table 3. All cases have a Jonswap frequency spectrum combined with directional spreading function with a mean incidence angle of 0° (Figure 4a):

$$D(\theta) = \cos^s(\theta) \qquad (23)$$

where s is the spreading index. A measure of the directional spreading, DSPR, is given by [*Kuik et al.*, 1990]:

$$\text{DSPR} = \sqrt{\int_{\pi/2}^{\pi/2} (2\sin(\theta/2))^2 D(\theta)d\theta} \qquad (24)$$

Bottom changes are computed over a period of approximately 4 days, which is typically a period in which an initially alongshore uniform beach (2-D) can change into a more complex 3-D beach [*Ranashinge et al.*, 1999]. The model parameters used throughout the 2-D computations are the same as used for modeling the accretive conditions observed during test 1C of the LIP11D experiment (see Table 2). The morphological time step was varied to assess its effect on the resulting morphodynamics. A large morphological time step allows for less computational time, however the results may become less accurate. For the cases presented here, there were negligible differences for a morphological time step of 1.5 hours (T_{flow} = 15 min. and
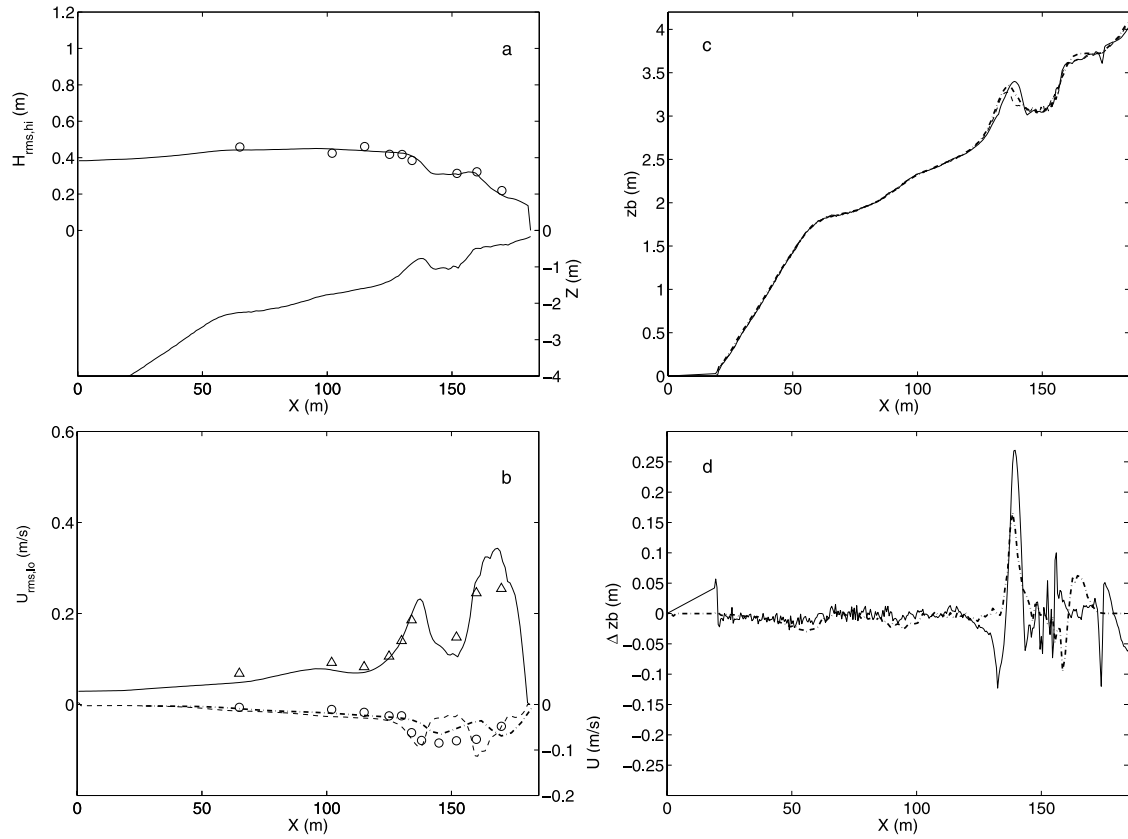
Figure 3. Test 1C. (a) Computed (solid line) and measured (circles) $H_{rms,hi}$. Bottom profile given as a reference. (b) Computed (solid line) and measured (triangles) $U_{rms,lo}$ and mean flow with (dash-dotted line) and without (dashed line) breaker delay compared to measurements (circles). (c) Initial (dashed line), measured (solid line), and computed (dash-dotted) bottom profiles after 14 hours. (d) Computed (dash-dotted) and measured (solid) bed level changes after 14 hours.

T_{morf} = 6) and 3 hours (T_{flow} = 15 min. and T_{morf} = 12) respectively, over a four day period. The low-frequency and high-frequency motions are partitioned at 0.04 Hz. The hydrodynamic time step is set at 2.4 seconds s, giving a minimum of ten points to represent the infragravity waves. Utilizing smaller time steps to represent the wave group conditions gave similar results in the hydro- and morphodynamics. A variable cross-shore grid is used with a coarser grid offshore (Δx < 25 m) and a higher-resolution grid within the surf zone (Δx < 5 m) where large gradients in wave and flow conditions are expected to occur. The alongshore grid spacing is kept constant at 10 m.

4.2. Boundary Conditions

[30] The surface elevation at the offshore boundary is constructed from a single summation, random phase model following *Van Dongeren et al.* [2003]. A random phase, ϕ_j, is assigned to each spectral frequency component $\hat{\eta}_j$ selected from the Jonswap spectrum, and the linear dispersion relation is utilized to relate the wave number k_i to the angular frequency ω_j:

$$\eta(x,y,t) = \sum_{j=1}^{N} \hat{\eta}_j e^{i\cdot(\omega_j t - k_{j,x}x - k_{j,y}y + \phi_j)} + * \qquad (25)$$

where the corresponding individual incidence angle is obtained from a probability function based on the directional distribution function, $D(\theta)$ (Figure 4a), and $*$ represents the complex conjugate. The corresponding wave envelope, A, is obtained with a Hilbert transform of the surface elevation (Figure 4b) and used to construct the wave group varying energy signal at the offshore boundary:

$$E(0,y,t) = \frac{1}{2}\rho g A^2(y,t) \qquad (26)$$

which is then low-pass filtered with a cut-off frequency of 0.04 Hz. The accompanying incoming bound infragravity wave has been ignored. The small free infragravity waves

Table 3. Parameter Settings for 2-D Morphodynamic Computations

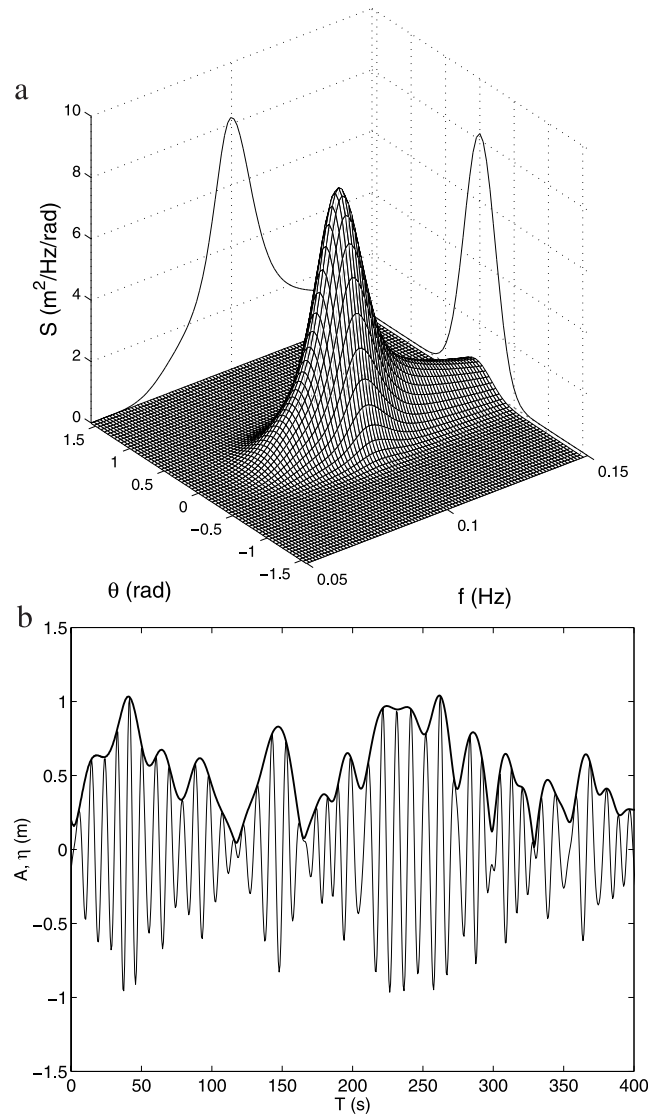| Parameter	H_{rms}	T_p	DSPR, deg
Test 001	1.0	10.0	0
Test 002	1.0	10.0	12.2
Test 003	1.0	10.0	15.5
Test 004	1.0	10.0	21.6
Test 005	1.0	10.0	8.0
Test 006	1.0	10.0	5.7
Test 007	1.0	10.0	1.8
Test 008	1.0	10.0	0.6

Figure 4. (a) Frequency directional spectrum for test 002 with a projected Jonswap frequency distribution and directional distribution. (b) Example of wave envelope time series test 002 (thick line) and underlying surface elevation (thin line).

thus generated at the offshore boundary (with velocities of O(0.001) m/s) are expected to have a negligible influence on the resulting morphodynamics. The offshore and shoreline boundary conditions are identical to the 1-D computations, i.e., a Riemann boundary offshore and a zero flux boundary at the shoreline defined by a minimum water depth of 0.2 m. The lateral boundaries are fully reflective, consistent with an embayed beach.

4.3. Initial Bathymetry

[31] The morphodynamic computations consider an embayed, single barred beach with an alongshore length of 1500 m and a cross-shore extent of approximately 1200 m with an offshore depth of 8 m. Following *Roelvink* [1993b], the initial alongshore uniform profile is based on an equilibrium beach profile given according to a simple power curve [e.g., *Bruun*, 1954; *Dean*, 1977]:

$$z = z_r - A_z(x - x_r)^b \qquad (27)$$

with A_z a dimensional constant and b an exponent, z_r a reference height at position x_r and the cross-shore coordinate x is positive in the offshore direction, to which a bar has been added:

$$z_b = z - A_b e^{-\left(\frac{x_{max}-x}{R_b}\right)^b} \cos\left(2\pi\frac{x - x_b}{L_b} - \phi_b\right) \qquad (28)$$

where A_b is the maximum bar amplitude, x_b the location of the maximum bar amplitude, R_b the relaxation length, L_b the bar spacing in case of multiple bars and ϕ_b the bar phase shift. The parameter setting for the initial cross-shore bottom profile used in the present test cases (Table 4) results in a bar trough profile (see Figure 5a) resembling observations at Duck, North Carolina [*Thornton and Kim*, 1993].

4.4. Initial Hydrodynamics on a Fixed Alongshore Uniform Bathymetry

[32] The default case, to which the other computational results will be compared is test 002 (see Table 3), corre-

Table 4. Constants for Bottom Profile Generation

Variable	Value
A, m	1.4
b	0.323
z_r, m	6
x_r, m	0
A_b, m	1.0
L_b, m	200
R_b, m	100
x_b, m	150
ϕ_b	$-\frac{\pi}{4}$

sponding to relatively narrow banded (both in frequency and direction) long period swell waves with a short-wave height, $H_{rms,hi}$, of 1 m at the offshore boundary and a peak period, T_p, of 10 seconds s. The mean wave direction is normally incident with a directional spreading of 12.2°. The offshore wave energy time series repeats every 150 min. First, the hydrodynamics are examined on the initial fixed bathymetry, i.e., computations are carried out without sediment transport to examine preferential length scales in the wave group-induced hydrodynamics that could trigger the morphological response.

[33] The computed mean wave transformation for test 002 shows a reduction in wave height over the bar due to wave breaking, cessation of breaking in the trough, followed by additional dissipation close to the shore line (Figure 5a). The corresponding low-frequency wave height, $H_{rms,lo}$, has a local maximum at the shoreward side of the bar and another maximum at the shore line where it exceeds the incident swell wave height.

[34] The cross-shore low-frequency velocity, $U_{rms,lo}$, has a local maximum located at the bar crest and another close to the shoreline (Figure 5b) with velocities exceeding 0.75 m/s. The alongshore low-frequency velocity, $V_{rms,lo}$, is significantly smaller, indicating the predominance of shore normal infragravity waves. In the alongshore direction, along the bar crest (Figure 5c), both $U_{rms,lo}$ and $V_{rms,lo}$ have little short scale structure, i.e., no evidence of a dominant standing edge wave mode. On a larger scale, the reflections of free infragravity waves at the sidewalls cause the increase in $U_{rms,lo}$ at both sides compared with the center region.

[35] A time stack of the energy modulation in the cross shore, i.e., variations with respect to the local mean wave energy expressed by ΔE, along a central cross-shore transect shows a sequence of wave groups incident on the beach (Figure 6a), with decreasing speed as the water depth decreases (i.e., increased curvature of the tracks). The modulation decreases strongly once the wave groups pass over the bar crest and wave breaking becomes important. Groups of higher waves break further offshore than the lower groups, resulting in a moving breakpoint position, thus contributing to the generation of infragravity waves [*Symonds et al.*, 1982]. The corresponding infragravity surface elevation (see Figure 6b) consists of both incident (sloping upward in the negative x direction) and reflected waves (sloping upward in the positive x direction). Offshore ($x > 1100$ m) the outgoing waves are dominant, given the mostly upward sloping contours. Moving toward the shore, the amplitude of the incident infragravity waves increases strongly with decreasing depth, thus resulting in an increased contribution of the incident infragravity waves

to the total infragravity motion. The strong amplification of the incident infragravity waves is due to the interaction of the incident wave groups and bound infragravity waves, which shoal faster than free infragravity waves as the water depth becomes less [*Longuet-Higgins and Stewart*, 1964].

[36] Frequency alongshore wave number ($f - k_y$) energy density spectra are calculated by performing a 2-D-FFT (in alongshore space and time) on both the 150-min cross-shore and alongshore velocity time series in an alongshore array (at $X = 190$ m; see Figure 5), divided into 15-min subseries resulting in 20 degrees of freedom (Figures 7a and 7b). Most infragravity energy density in the cross-shore velocity $f - k_y$ spectrum is within the leaky mode area (indicated by the dashed lines in Figure 7a). The lack of energy density around $f = 0.016$ Hz is associated with the nodal structure of the cross-shore standing infragravity waves, where the u contributions of the incident and reflected infragravity waves for this frequency are out of phase at this location.
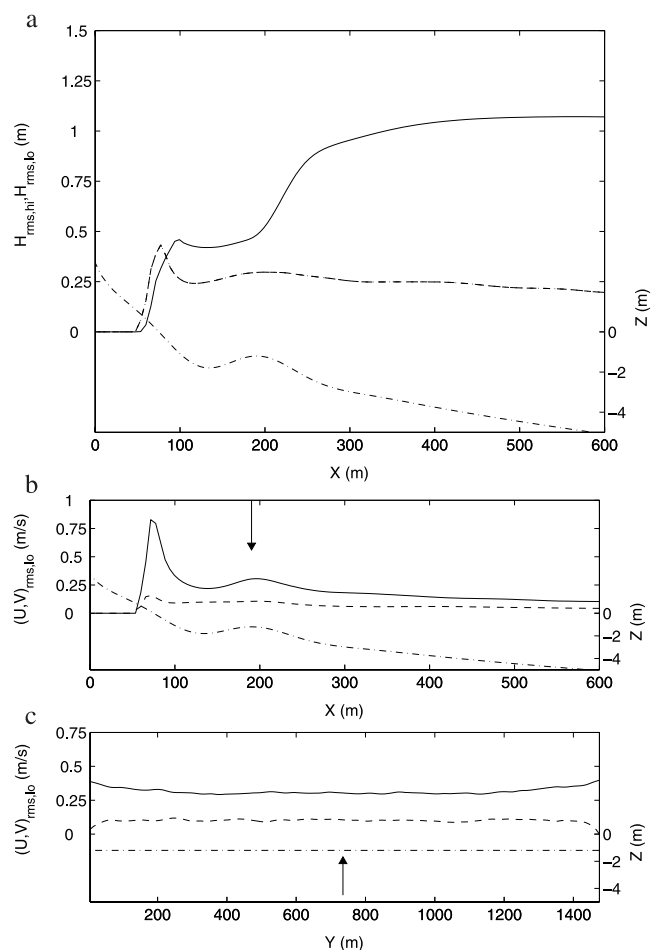

Figure 5. Initial conditions for test 002. (a) Bottom profile (dash-dotted line) and corresponding $H_{rms,hi}$ (solid line) and $H_{rms,lo}$ (dashed line) at the central cross-shore transect (at $Y = 810$ m). (b) Bottom profile (dash-dotted line) and corresponding $U_{rms,lo}$ (solid) and $V_{rms,lo}$ (dashed) at the central cross-shore transect. (c) Bottom profile (dash-dotted line) and corresponding $U_{rms,lo}$ (solid) and $V_{rms,lo}$ (dashed) along the bar crest (at $X = 190$ m). Position of transects indicated by arrows.
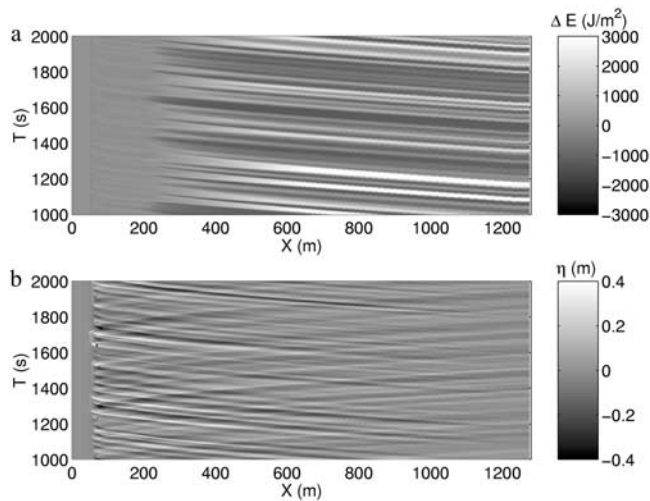
Figure 6. Initial conditions for test 002. (a) Computed modulated wave energy, ΔE, with respect to local mean energy at a central cross-shore transect as function of time. (b) Corresponding computed infragravity surface elevation, η, as function of time. The shoreline is located at the left.

The concentration of energy density in v at $f = 0.016$ Hz is also related to the nodal structure, with the v contributions of the incident and reflected infragravity waves being in phase at this location (Figure 7b). The alongshore velocity $f - k_y$ spectrum does show the presence of edge waves (i.e., outside the leaky wave curves), though the intensity is significantly less than obtained for the cross-shore infragravity motions (compare Figures 7a and 7b). This lack in edge wave energy density can be explained by the fact that the mean incidence angle of the short waves is shore normal. The theoretical edge wave curves for a plane sloping beach of 1:100 suggest that the computed energy density outside the leaky wave band corresponds predominantly to higher mode edge waves ($n > 3$). The alongshore edge wave velocity energy density is smoothly distributed over both frequency and alongshore wave number space, i.e., there is no evidence of preferential edge wave forcing and consequently no preferential length scale. However, the hydrodynamic response at the very low frequencies outside the infragravity band (i.e., outside the zero mode edge wave curves) displays energy density with relatively short alongshore length scales for both the cross-shore and alongshore motions (Figures 7a and 7b and in more detail in Figure 8), which will be discussed in detail below.

[37] A 2-D-FFT of the wave energy time series at the offshore boundary shows the frequency and wave number distribution of the wave group energy (Figure 7c) forcing the hydrodynamic motions. The alongshore wave number distribution of the wave group energy is significantly broader than the observed response in the infragravity velocities for frequencies higher than 0.0033 Hz (Figures 7a and 7b). This is expected through nonlinear coupling [*Herbers et al.*, 1995], which decreases rapidly with increasing difference angle (corresponding to large k_y values) between the short-wave components and the underlying infragravity waves. For the very low frequency band (0.0011 Hz < F < 0.0022 Hz), both the forcing (Figure 7c) and response

(Figure 8) have significant energy density at relatively short alongshore wavelengths (outside the infragravity band). At the lowest-frequency band ($f < 0.0011$ Hz), the forcing is negligible outside the infragravity band (Figure 7c), however the velocity response is strong over a wide range of k_y values (Figure 8).

[38] The strong response for the very low frequencies (0.0011 Hz < F < 0.0022 Hz), typically associated with shear instabilities in the longshore current [*Oltman-Shay et al.*, 1989], seems odd given the fact that the mean wave incidence angle is zero, and consequently there is no longshore current present. Still, the temporal and spatial distribution of the wave group energy varies due to the presence of directional spreading in the short waves. *Fowler and Dalrymple* [1990] showed that spatially and temporally varying wave group energy made up of a pair of intersecting plane wave trains of slightly different frequency could generate slowly alongshore migrating circulation cells, at low frequencies. This process is demonstrated by considering the wave energy made up of two intersecting wave trains of slightly different frequency, $f_1 = 0.101$ Hz and $f_2 = 0.099$ Hz, and nearly opposite directions, $\theta_1 = -12.25°$ and $\theta_2 = 12.5°$. This yields a spatially varying energy pattern (see Figure 9a) that moves slowly in the downward alongshore direction, where the alongshore length scale is determined by the difference wave number made up by the two wave trains:

$$\Delta k_y = k_1 \sin(\theta_1) - k_2 \sin(\theta_2) = -0.0318 \text{m}^{-1} \qquad (29)$$

corresponding to a alongshore wavelength of 197.6 m, and the timescale is determined by their difference frequency:

$$\Delta f = f_1 - f_2 = 0.002 \text{Hz} \qquad (30)$$

corresponding to a period of 500 seconds s. The radiation stresses associated with the wave groups and the resulting pressure gradients generate the slowly migrating rip currents (see Figure 9b), with the same timescale, Δf, and short alongshore length scale, Δk_y, as the wave groups forcing it, propagating $\frac{\Delta f}{\Delta k_y} = 0.063$ m/s in the downward direction. Deviations in the circulations occur near the lateral boundary, though these effects do not affect the interior flow domain (i.e., the vortices do not "reflect" from the lateral boundaries).

[39] The mechanism proposed by *Fowler and Dalrymple* [1990] can also generate motions at (relatively) higher infragravity frequencies. However, the energy associated with those motions quickly drops off, as can be seen from the expression for the cross-shore low-frequency velocity on a alongshore uniform beach [*Reniers et al.*, 2002b, equation (A7)]:

$$\hat{u} = \frac{-g \frac{d\hat{\eta}}{dx} - \hat{F}_x}{(i\omega)} \qquad (31)$$

where the hat indicates a complex amplitude, $i = \sqrt{-1}$, ω the radial frequency of the very low frequency motion, and both bottom friction and lateral mixing have been ignored. Equation (31) shows that for a given forcing, the energy density of the very low frequency motions drops off as ω^{-2}, which suggests that the contributions of this mechanism to
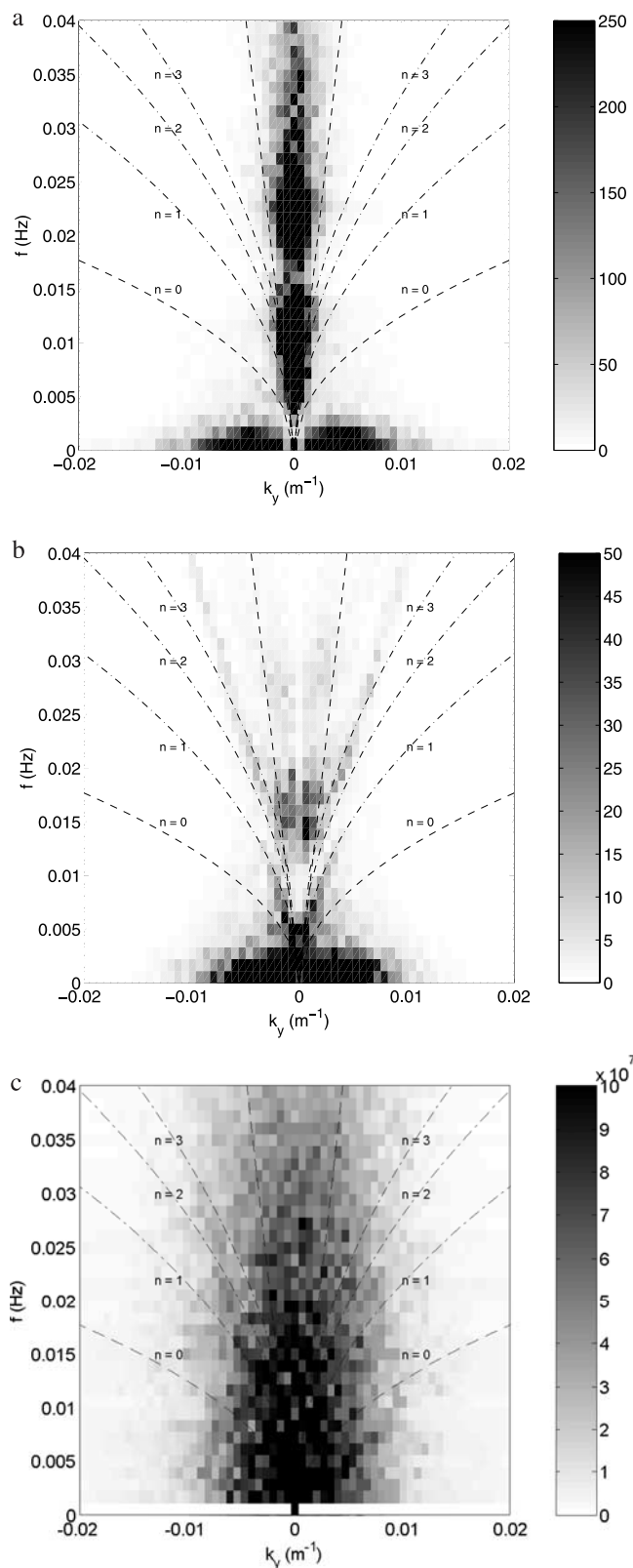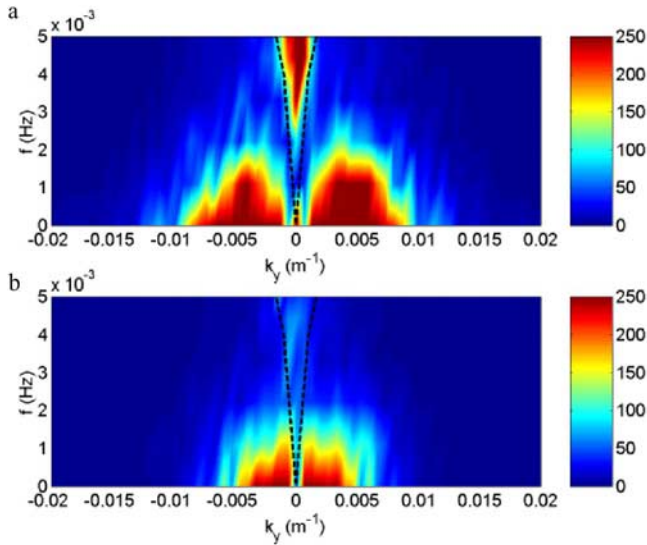
Figure 7. (a) Cross-shore low-frequency velocity $f - k_y$ energy density spectra $(m^2/s^2/Hz/m^{-1})$ for test 002 at the alongshore transect (at $X = 190$ m) for the initial fixed bathymetry. (b) Similar for the alongshore low-frequency velocities at the alongshore transect. (c) The $f - k_y$ spectral density of the wave group energy $(J/m^2/Hz/m^{-1})$ calculated at the offshore boundary. The leaky mode regime is indicated by the area enclosed by the dashed lines and the edge wave dispersion curves for a 1:100 plane slope are indicated by the dash dotted lines.

Figure 8. (a) Very low frequency cross-shore velocity $f-k_y$ energy density spectra ($m^2/s^2/Hz/m^{-1}$) for test 002 at the alongshore transect (at $X = 190$ m) for the initial fixed bathymetry. (b) Similar for the alongshore velocities at the alongshore transect. The zero-mode edge wave dispersion curves for a 1:100 plane slope are indicated by the dashed lines.

the low-frequency velocity spectrum are predominantly within the lowest frequencies.

[40] A special case occurs if the frequencies of the two wave trains are equal, and the circulation pattern becomes stationary [*Dalrymple*, 1975]. The wave group energy forcing this particular scenario would show up at relatively large alongshore wave numbers within the lowest-frequency bin ($f < 0.0011$ Hz). This is not the case here (Figure 7c); hence the mechanism outlined by *Dalrymple* [1975] does not explain the strong velocity response at the lowest-frequency bin.

[41] *Ryrie* [1983] considered the momentum associated with a single wave group that is sharply peaked in the alongshore direction, and showed that this wave group through variations in momentum generates both transient motions (such as edge waves that disperse away) and a steady circulation, which is left behind. This circulation is then slowly dissipated due to bottom friction giving it a very low frequency signature, i.e., a much longer timescale than the wave group forcing it. This very low frequency behavior is demonstrated by the computed quasi-steady circulation generated by a single wave group of limited alongshore length and time (Figure 10a), after the wave group has been dissipated due to wave breaking and transient motions dispersed (Figure 10b). The alongshore spacing of the circulations and corresponding vorticity, expressed by

$$Q = \frac{\partial v}{\partial x} - \frac{\partial u}{\partial y} \qquad (32)$$

are related to the alongshore length of the wave group (compare Figures 10a and 10b). In reality wave groups are not necessarily sharply peaked in the alongshore direction,

and as such they typically generate two circulation cells of opposite vorticity [*Peregrine*, 1998; *Bühler and Jacobson*, 2001], as opposed to a single circulation cell considered by *Ryrie* [1983] (Figure 10b). In the case of two wave groups that have been offset in space and time (Figure 10c), the interaction of vortices can lead to narrow, offshore-directed quasi-steady flows as two cells of opposite vorticity pair up and slowly dissipate (Figure 10d).

[42] The present modeling effort considers a large number of temporally and spatially varying wave groups entering the surf zone. In that case the temporal scale of the very low frequency circulations is determined by the individual contributions of each incident wave group to the existing circulation. This is illustrated in Figure 11, where the cross-shore velocity response within the surf zone to a sequence of incident wave groups (Figure 11a) shows the infragravity velocities (on the wave group timescale) superimposed on the slowly varying circulation velocity (Figure 11b). This response is examined in more detail by considering a sequence of snapshots of the vorticity field and the corresponding slow circulations (Figure 11c). Given the randomness of the wave field, the individual wave groups have significant variation in energy (Figure 11a). This results in a strong spatial modulation of the vorticity field within the surf zone (Figure 11c), where strong vortices can be generated by wave groups with a high-energy content, a sequence of smaller groups breaking at the same location or the merging of weaker vortices. Vortex dynamics then determine the slow flow response, where the pairing of two strong vortices of opposite vorticity results in strong offshore directed flows (see Figure 11c near cross sections at $Y = 640$ m and $Y = 820$ m). The temporal scale of these vortex pairs, and corresponding offshore directed flows, depends on dissipative effects such as bottom friction, the interaction with other existing vortices, and the contributions of new breaking wave group-induced vortices. Only the latter occur on the wave group timescale, and then only the vortices generated by energetic wave groups are strong enough to alter/destroy the existing vortex-pair. Given the
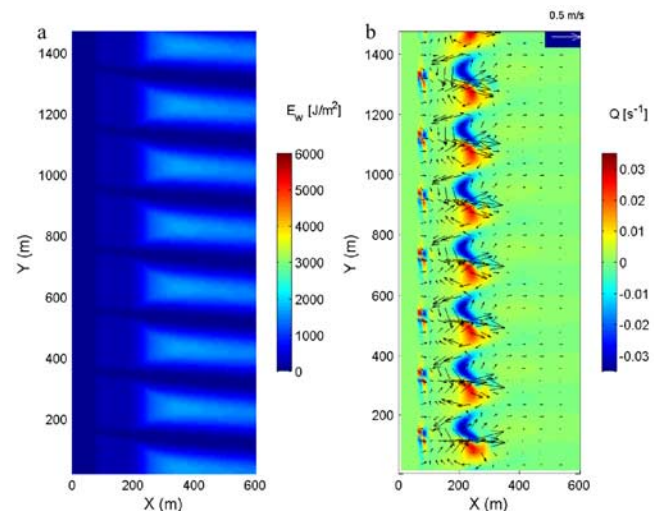

Figure 9. (a) Snapshot of wave group energy made up of two intersecting wave trains at T = 30 min. (b) Snapshot of corresponding vorticity and velocity field at T = 30 min.
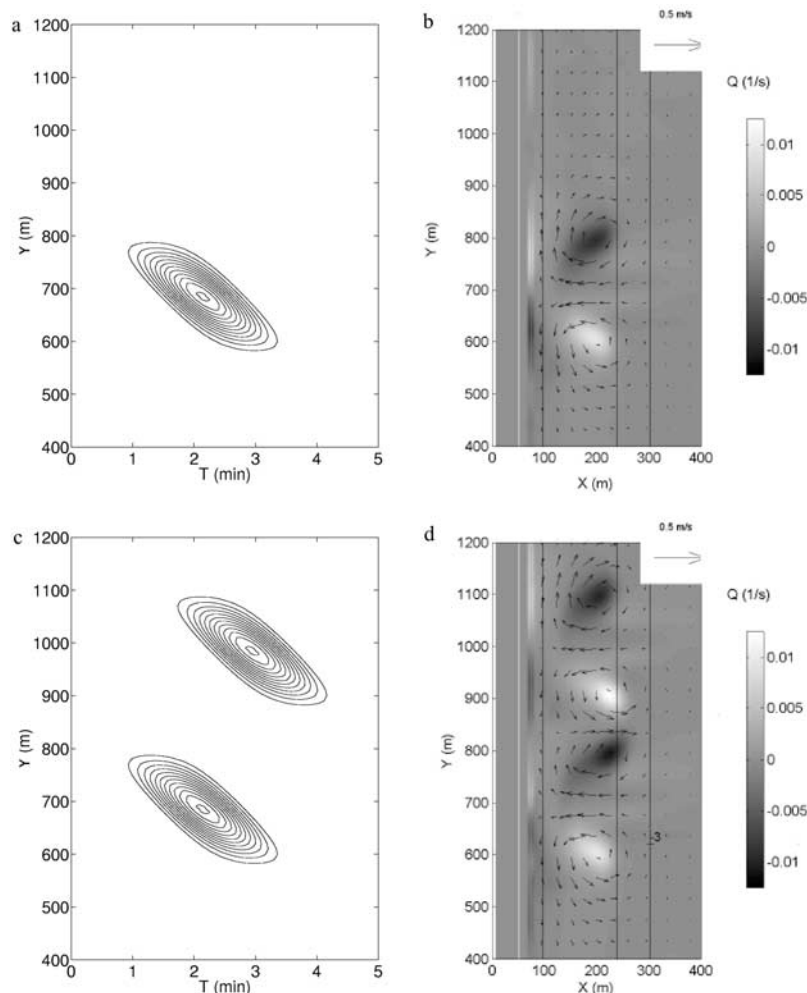
Figure 10. Vortex dynamics (within part of the domain). (a) Temporal and spatial distribution of wave energy at the offshore boundary, in 100 J/m^2 contour intervals, for a single wave group. (b) Quasi-steady circulation and corresponding vorticity after 15 min. (c) Temporal and spatial distribution of wave energy at the offshore boundary, in 100 J/m^2 contour intervals, for two wave groups. (d) Quasi-steady circulation and corresponding vorticity after 15 min.

randomness of the incident waves, the more energetic wave groups are generally separated by many less energetic wave groups (Figure 11a) allowing these flows to persist over many wave groups resulting in timescales that are much longer than the temporal scale of the wave groups. In contrast, the alongshore length scales remain similar to the wave group length scales that generated the strong vortices (Figure 12a). Consequently the width of the along-shore wave number distribution of the quasi-steady flows is similar to the width of the wave group forcing (Figure 12a), which in turn is a function of the directional spreading of the short waves. A sequence of incident wave groups thus results in an inhomogeneous quasi-steady flow field within the surf zone with length scales similar to the incident wave groups. An example of such a circulation pattern, with alongshore length scales of approximately 200 m, is shown in Figure 12b, based on a 15 min average of the computed flow field for test 002 (note that the offshore flows at $(Y) = (640 \text{ m})$ and $(Y) = (820 \text{ m})$ observed in Figure 11c are present). This 200 m length scale corresponds to the peak

energy density of the cross-shore velocities centered at $|k_y| = 0.005 \text{ m}^{-1}$ in the lowest-frequency bin (Figure 8a). The circulation patterns mostly disappear if the averaging period is increased to 2.5 hours (see Figure 12c), i.e., much longer that the temporal scale of the strong vortices, which occur randomly alongshore on the alongshore uniform fixed beach.

[43] The approach utilized here, i.e., the computed evolution of temporally and spatially varying wave group energy owing to an incident directional short-wave spectrum over a variable bathymetry forcing low-frequency motions, is a more general description of the hydrodynamic response to wave group forcing. As such it includes the two-wave component mechanism proposed by *Fowler and Dalrymple* [1990] and the solitary group mechanisms by *Bühler and Jacobson* [2001]. Also note that the quasi-steady circulations, or very low frequency motions considered here, have been observed in nature on both planar beaches ([*Tang and Dalrymple*, 1989], and more complex beaches [*MacMahan et al.*, 2003; J. MacMahan et al., Very
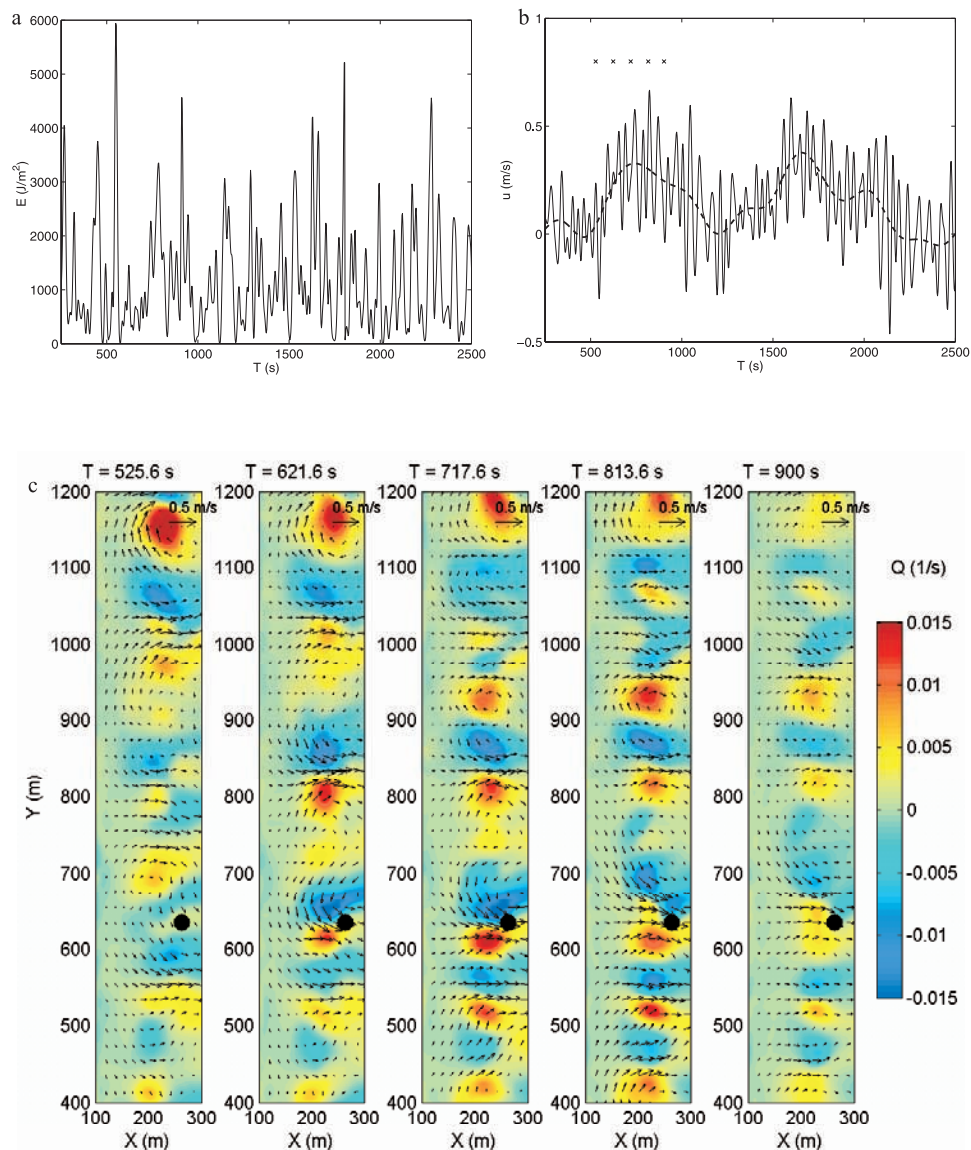
Figure 11. (a) Wave energy for test 002 at the offshore boundary at $Y = 640$ m. (b) Corresponding cross-shore velocity at a point within the surf zone $((X, Y) = (264, 640)$ m, i.e., black dot in the Figure 11c), showing infragravity waves (solid line) superimposed on the slowly varying circulation velocity (dashed line). (c) Snapshots of low-passed ($f < 0.004$ Hz) vorticity and flow velocity at 96 s intervals (indicated by the crosses in Figure 11b). Reference velocity denoted by arrow in upper right corner of each plate.

low frequency options on a complex beach, submitted to *Journal of Geophysical Research*, 2002] for which the latter have been successfully modeled [*Reniers et al.*, 2002a]. As a result of the vortex dynamics, the quasi-steady (or very low frequency) velocity response within the surf zone becomes quite complex and the temporal relationship with the offshore wave groups forcing the vortices is no longer straightforward.

[44] In conclusion, there is no preferential length scale in the computed infragravity motions that could trigger a quasi-periodic morphological response in the nearshore. However, the wave group-induced vortices and corresponding quasi-steady flow circulations, associated with the spatially varying wave groups, do exhibit a preferential length scale, that is O(200) m. It is shown below that on a movable bed,

there is a coupling of the vortices with the morphology resulting in a quasi-periodic morphological response.

4.5. Morphodynamic Coupling

[45] In the following, the bathymetry is allowed to evolve to examine the morphodynamic response under wave group forcing. The bathymetric changes after 45 hours (Figure 13a) show a meandering deposition pattern around the bar crest. The erosion patterns are more isolated, with maximums at approximately 200 m alongshore intervals, suggesting the initial evolution of a rip channeled beach. This evolution is confirmed by the computed erosion/deposition pattern after 90 hours (Figure 13b), showing seven rip channels with an average alongshore spacing of O(220) m, though the actual alongshore distribution is
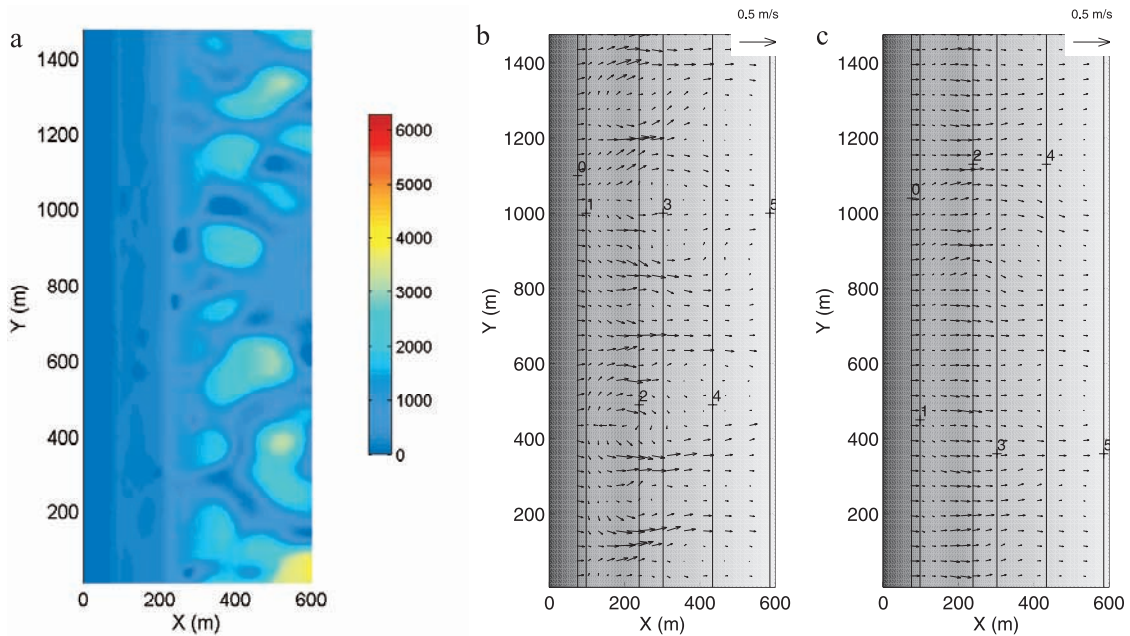
Figure 12. (a) Snapshot of incident wave energy in J/m^2 for test 002. (b) Computed 15-min averaged flow field (indicated by the arrows) for test 002 over the initial fixed alongshore uniform bathymetry. (c) Similar for 150-min average. All contour intervals in meters.

irregular with a maximum spacing of $O(320)$ m and a minimum spacing of $O(180)$ m. The width of the rip channels is O(50) m, thus typically smaller than the width of the adjacent shoals. The mean flow pattern superimposed on the bathymetry (Figure 13c) shows an onshore flow on the shoals that diverges close to shore into feeder channels, which in turn support the offshore directed flow in the relatively narrow rip channels.

[46] The time evolution of the bed level at the alongshore transect shows the growth of relatively narrow rip channels and broad shoals (Figure 14a). Initially, i.e., up to $T = 30$ hours, the bed level at all locations increases, corresponding to an accreting bar system with a mild growth rate. After $T = 30$ hours, the bed at the future rip channels starts to erode, and the growth rate rapidly increases. After $T = 60$ hours, the bed level at the shoals stays more or less constant, whereas the rip channels continue to deepen. This is confirmed by examining the bed evolution on the shoal (Figure 14b), which shows a rapid increase in the growth rate around $T = 40$ hours, which levels off around $T = 50$ hours. The concurrent hourly averaged cross-shore velocity on the (future) shoal is offshore directed during the first 25 hours (Figure 14d), corresponding to a return flow (undertow). After that time the flow reverses and the velocity quickly increases until approximately $T = 50$ hours. Once the cross-shore flow velocity becomes significant, i.e., around T
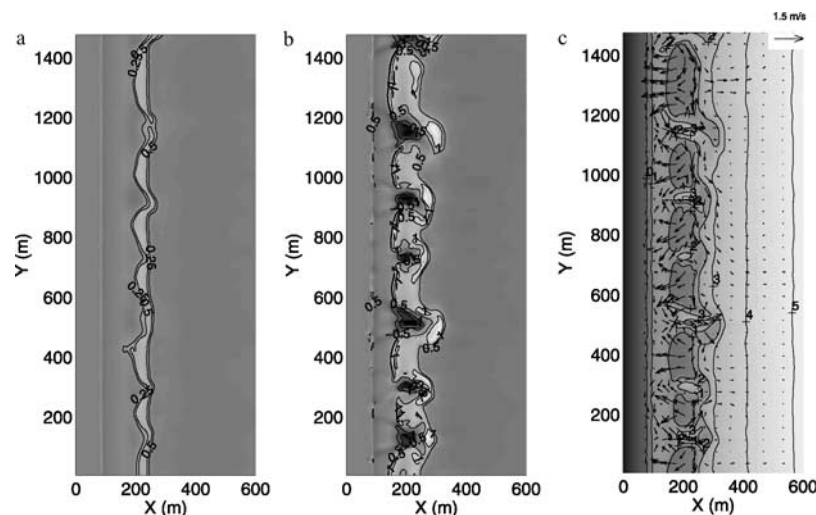

Figure 13. (a) Computed erosion/deposition after 45 hours for test 002. (b) Similar after 90 hours. (c) Mean current velocity superimposed on the bathymetry after 90 hours. All contour intervals in meters.
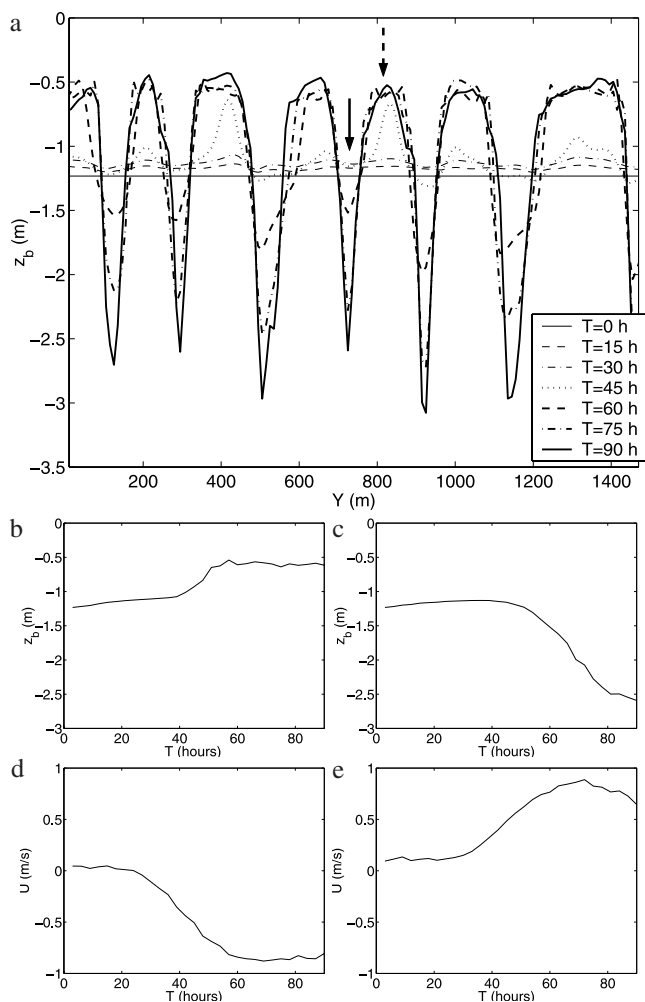
Figure 14. Bathymetric evolution. (a) Bed level at the alongshore transect (at $X = 190$ m) at different times T (in hours). (b) Temporal evolution of the bottom at the shoal (at $(X, Y) = (190$ m, 810 m), dashed arrow). (c) Temporal evolution of the bottom within a rip channel (at $(X, Y) = (190$ m, 720 m), solid arrow). (d) and (e) Corresponding hourly averaged cross-shore velocities (positive offshore).

= 40 hours, the shoal's bed-evolution quickly increases (compare Figures 14b and 14d). The bed-level within the rip-channel also shows a strong increase in the growth rate around $T = 40$ hours, however leveling off is not apparent (Figure 14c), though the growth rate declines within the last 10 hours. The concurrent hourly averaged cross-shore velocity within the (future) rip channel shows an increase around $T = 25$ hours, which coincides with the flow reversal on the shoal, and quickly increases until $T = 70$ hours as the evolving rip channels start attracting more and more discharge. As the rip channels continue to deepen, and the slopes of the rip channels become steeper, wave diffraction is expected to become important. In addition, the strong rip currents that develop within the rip channels (Figure 14e) are expected to affect the propagation of the incident waves through wave-current interaction [*Yu and Slinn*, 2003]. However, diffraction and wave-current interaction only are expected to become important once the rip channels are well established and not

during the initial evolution of the rip channels. As a consequence the bathymetry is expected to evolve differently from the present computations once these effects become important.

[47] It is interesting to note that the present final bathymetry shows strong similarities with the results obtained by *Damgaard et al.* [2002], with similar alongshore spacings for the rip channels and similar bed level changes on both shoals and within the rip channels (compare Figure 6 of Damgaard et al. with Figure 14a). However, the timescale of the morphological evolution is significantly faster in the present computations due to the presence of additional cross-shore sediment transport contributions associated with both wave asymmetry and wave-induced mass flux, which are not present in the computations of *Damgaard et al.* [2002]. In addition, the alongshore transect of the final bathymetry is smoother, i.e., the 'horns' at the edges of the rip channels present in the computations of *Damgaard et al.* [2002], and also visible at $T = 60$ hours in Figure 14a, are no longer present in the final bathymetry due to the presence of infragravity waves (discussed below).

[48] In the final bathymetry, i.e., at $T = 90$ hours, the cross-shore transect is positioned on a shoal (Figure 15c). Wave dissipation occurs primarily on the shallow shoal, reducing the wave height by 75% (Figure 15a). The cross-shore distribution of the infragravity wave height is similar to the initial conditions (Figure 5), accompanied by an approximate 20% increase in the intensity over the bar crest. The cross-shore and alongshore distribution of the low frequency velocities has changed considerably with respect to the initial conditions (Figures 15b and 15c). In the cross shore, the contribution of the alongshore velocity component to the total low frequency motion has increased, with a maximum at the seaward side of the shoal. The magnitude of the cross-shore low-frequency velocities also increased with respect to the initial conditions. In the alongshore direction, strong variation in both $U_{rms,lo}$ and $V_{rms,lo}$ is present, with local minima coinciding with the rip channel locations.

[49] The frequency, alongshore wave number plots show the increased contribution of trapped edge waves to the total infragravity motions (compare Figure 16 with Figure 7). The cross-shore infragravity motion is still dominated by cross-shore standing waves, though contributions outside the leaky bandwidth are clearly present as well (Figure 16a). The alongshore infragravity motion shows a preferential length scale in the order of 220 m at a frequency of approximately 0.02 Hz where most of the edge wave energy density is concentrated (Figure 16b), which corresponds to the observed rip channel spacing. This indicates there is a coupling between the edge wave field and the underlying complex bathymetry, something that has been observed under field conditions [*Wright et al.*, 1979].

[50] Even though the initial infragravity conditions showed no preferential alongshore length scale, the question remains whether the observed morphodynamic response is governed/influenced by the infragravity conditions through a positive feedback mechanism. To answer this question, a test without the infragravity velocity contribution in the sediment transport is examined by filtering the velocity time series used in the sediment transport equation, equation (13), with a 5-min moving average, thus retaining the quasi-
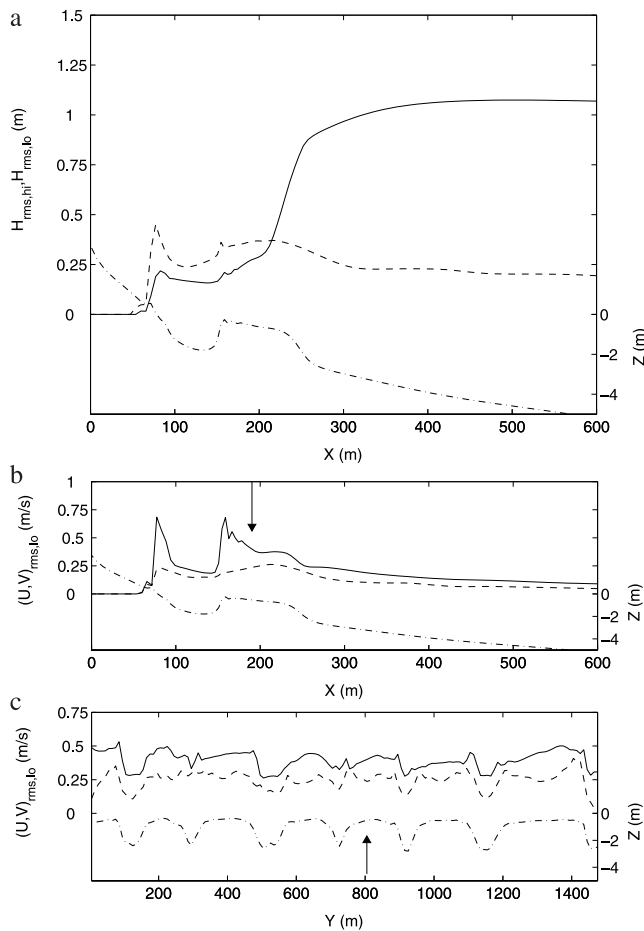
Figure 15. Final conditions for test 002. (a) Bottom profile (dash-dotted line) and corresponding $H_{rms,hi}$ (solid line) and $H_{rms,lo}$ (dashed line) at the central cross-shore transect (at $Y = 810$ m). (b) Bottom profile (dash-dotted line) and corresponding $U_{rms,lo}$ (solid) and $V_{rms,lo}$ (dashed) at the central cross-shore transect. (c) Bottom profile (dash-dotted line) and corresponding $U_{rms,lo}$ (solid) and $V_{rms,lo}$ (dashed) along the bar crest (at $X = 190$ m). Position of transects indicated by arrows.

steady circulations, but removing the infragravity contributions. The number of rip channels and their alongshore spacing in the final bathymetry is very similar to the case with infragravity waves included (compare Figure 17 with Figure 13c), though the actual shape of both shoals and rip channels can be quite different. The most prominent effect of including the infragravity waves in the sediment transport is to smooth the bathymetric changes, resulting in milder seaward slopes of the shoals. Therefore the present results suggest that infragravity waves are not required to generate the quasi-periodic alongshore patterns, and the observed preference in length scale for the edge wave motions is a result of the underlying bathymetry and not the other way around.

4.6. Effects of Directional Spreading

[51] The effects of directional spreading on the morphodynamic response are examined next. Different cases are examined in detail, starting with no directional spreading,

increasing directional spreading, and then decreasing directional spreading (see Table 3 for details).

[52] Considering the case without directional spreading first, i.e., normally incident wave groups constructed of a Jonswap spectrum, where the individual wave angle θ_j in equation (25) is set to zero. This means that initially there is no alongshore variation in the energy associated with the wave groups. Consequently there is no forcing of alongshore infragravity motions, and the resulting infragravity wave field is cross-shore standing only. Given the uniform conditions, the initial mean flow field has no alongshore variation either (see Figure 18a). Still, the computed bathymetric changes after 90 hours show multiple rip channels occurring approximately every 140 m (Figure 18d). Given the fact that initially there is no alongshore variation in the forcing conditions, these results suggest that the develop-
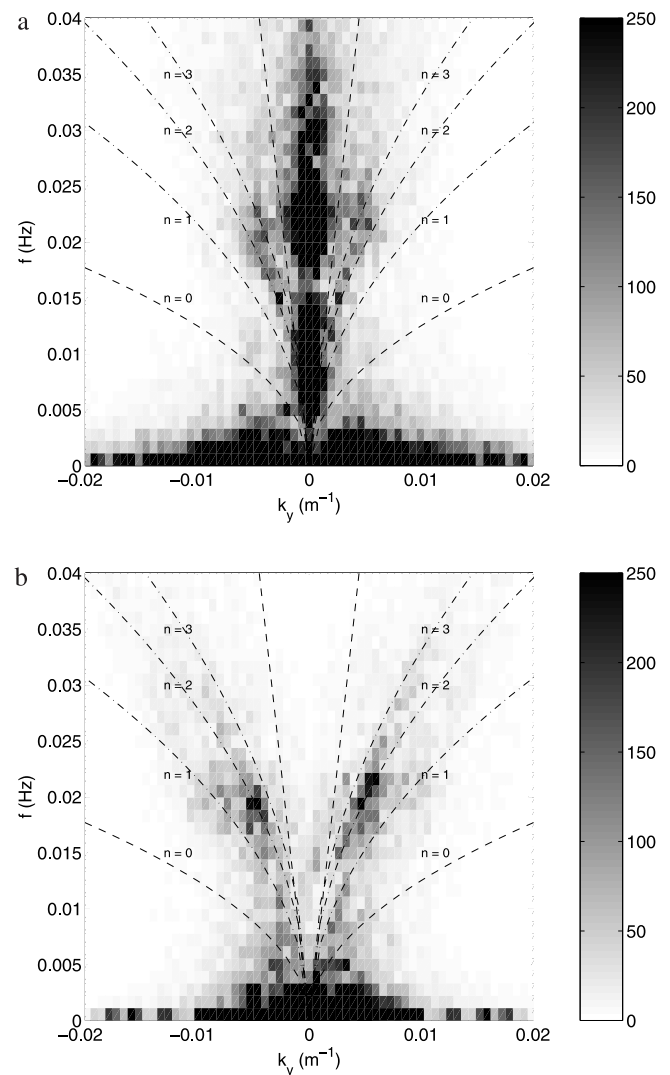

Figure 16. Frequency-alongshore wave number energy density spectra ($m^2/s^2/Hz/m^{-1}$) calculated at the alongshore transect for the final bathymetry. (a) Cross-shore infragravity velocities. (b) Alongshore infragravity velocities. The leaky mode regime is indicated by the area enclosed by the dashed lines and the edge wave dispersion curves for a 1:100 plane slope are indicated by the dash-dotted lines.
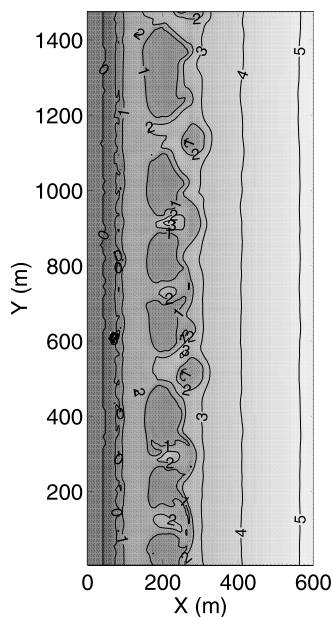
Figure 17. Computed bathymetry after 90 hours for test 002 without the infragravity velocity contribution in the sediment transport. All contour intervals in meters.

ment of the quasi-periodic, rip channeled beach for unidirectional normally incident waves is governed by the self organizing properties of the morphodynamic system, where small undulations in the bathymetry grow due to a positive feedback between the bed and the hydrodynamic conditions. The initial perturbations are due to small errors within the computations. To make sure that the morphodynamic response is not governed by lateral boundary effects, additional computations with a small random perturbation (less than 0.3 cm) added to the initial bottom were performed. This lead to similar results as for the unperturbed case, indicating that lateral boundary effects are not responsible for the bottom evolution within the interior.

[53] The directional spreading is increased to examine the effect of a relatively broad directional distribution (see Table 3, test 004). The bathymetric changes after 90 hours are quite similar to the results obtained for test 002, though with two additional rip channels resulting in an average alongshore spacing of $O(175)$ m, which is shorter than the results obtained for test 002 (compare Figure 18e and Figure 13c). These shorter length scales can also be observed in the mean circulation pattern for test 004 (Figure 18b). Decreasing the directional spreading results in longer alongshore length scales of the individual wave groups and consequently larger quasi-steady circulations (see Figure 18c), resulting in fewer rip channels with corresponding larger alongshore length scales in the order of $O(300)$ m (Figure 18f). These results suggest there is correlation between the length scales in the quasi-steady flow circulations and the alongshore spacing of the rip channels and shoals.

[54] The eventual alongshore position of the rip channels is a function of the randomness of the wave groups, where a specific sequence of wave groups creates an undulation in the bar topography big enough to change the wave and flow field. This initiates a positive feedback mechanism that

allows the undulation to grow in time, thus resulting in a quasi-forced beach response. Utilizing a different seed number to generate the offshore random phase wave group time series, equation (25), therefore results in different realizations of the beach response. To further test the correlation between directional spreading and alongshore spacing, 8 realizations for each case of directional spreading (see Table 3) were analyzed to get a stable estimate of the expected alongshore spacing of the rip channels. In addition, computations on the fixed initial alongshore uniform bathymetry were performed to estimate the alongshore length scales, L_y, of the quasi-steady circulations for each case of directional spreading:

$$L_y = \frac{\int_0^{0.0022 Hz} \int_{0.02 m^{-1}}^{-0.02 m^{-1}} S_{uu}\left(f, k_y\right) dk_y df}{\int_0^{0.0022 Hz} \int_{0.02 m^{-1}}^{-0.02 m^{-1}} k_y S_{uu}\left(f, k_y\right) dk_y df} \qquad (33)$$

to compare with the observed alongshore spacing of the rip channels.

[55] Without directional spreading the shortest alongshore rip channel spacing is obtained, whereas the theoretical alongshore spacing is infinitely long (Figure 19). Introducing a small amount of directional spreading (less than 2°) in the wave group forcing leads to a significant increase in the observed alongshore separation scale of the rip channels (Figure 19) as the morphodynamic response changes from self organizing (with corresponding short alongshore length scales) to being quasi-forced (with relatively large alongshore length scales associated with the quasi-steady circulations). For increased directional spreading, the quasi-steady circulations dominate the morphodynamic response, and the alongshore spacing of the rip channels is determined by the length scales of the quasi-steady circulations, and is therefore a function of the directional spreading of the short waves (Figure 19).

[56] Note that the quasi-steady circulations are only moderately affected by the lateral boundaries (Figure 9). It is therefore expected that the relation between directional spreading of the short waves and the resulting morphodynamic response will hold on both embayed and (semi-) infinite beaches.

5. Concluding Remarks

[57] A quasi-periodic morphodynamic response of the nearshore beach is obtained for wave group forcing made up of directionally spread incident short waves with a zero mean incidence angle on an initially alongshore uniform barred beach. The wave group hydrodynamics and sediment response is described using a numerical process model. The most prominent feature of the 2-D computations is the development of an alongshore quasi-periodic bathymetry of shoals cut by rip channels.

[58] Without directional spreading, the mean flow pattern is initially alongshore uniform. This changes once irregularities in the bathymetry (in this case associated with small errors in the computations) are large enough to attract more discharge, resulting in an alongshore periodic bathymetry corresponding to a self organizing beach response.

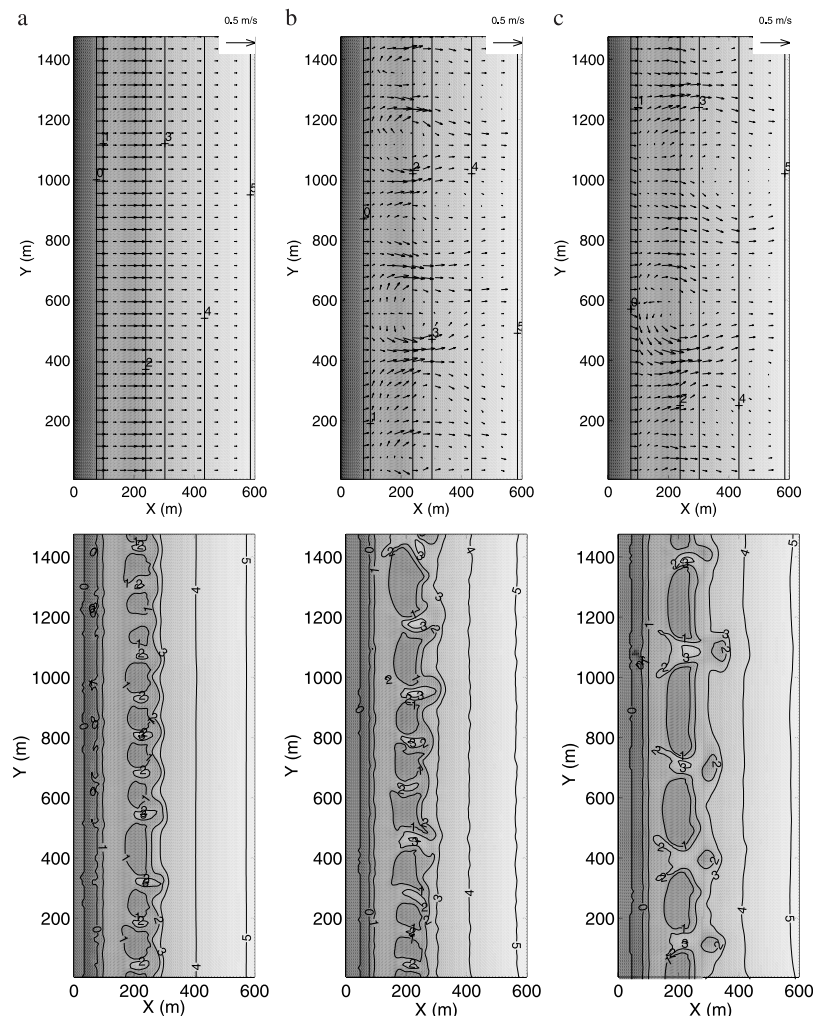[59] When directional spreading in the wave group forcing is introduced, the beach response changes from self

Figure 18. (a) 15-min averaged flow field for test 001 over initially alongshore uniform bathymetry (DSPR = 0°). (b) similar for test 004 (DSPR = 21.6°). (c) similar for test 006 (DSPR = 5.7°). (d)–(f) Corresponding bathymetry after 90 hours.

organizing to being quasi-forced with a rapid increase in the alongshore separation of the rip channels. A further increase in directional spreading leads again to smaller alongshore length scales. The reason for the observed difference in the alongshore separation of the rip channels for the different cases of directional spreading is the underlying quasi-steady circulation pattern on the initial (alongshore uniform) bathymetries. The presence of wave groups induces spatially varying mass and momentum fluxes and (alongshore) pressure gradients resulting in an inhomogeneous velocity field. The ensuing circulations depend on the alongshore length scales of the wave groups and thus the directional spreading of the short waves.

[60] The present results show that the computed infra-gravity velocity contribution is not required to generate the observed computed morphodynamic quasi-periodic response of the beach. Infragravity waves do play a role in the transport of sediment, where their main contribution in the cases considered here is to smooth the resulting bathymetric features. Similar conclusions were reached by *Roelvink* [1993b] on the basis of 1-D computations of infragravity waves and corresponding sediment transport.
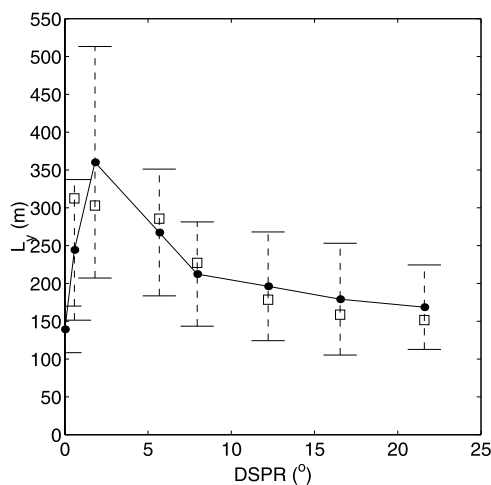

Figure 19. Average alongshore spacing (dots) of rip channels plus or minus the standard deviation as function of the directional spreading (DSPR) of the short waves. Corresponding alongshore length scales of the quasi-steady circulations given by the squares.

The observed coupling between edge waves on the final complex beach topography is a result of the underlying bathymetry and not the other way around.

References

Arcilla, A. S., J. A. Roelvink, B. A. O'Connor, A. Reniers, and J. A. Jimenez (1994), The Delta flume '93 experiment, in *Coastal Dynamics '94*, edited by A. S. Arcilla, N. C. Kraus, and S. J. F. Marcel, pp. 488–502, Am. Soc. of Civ. Eng., Reston, Va.

Barcilon, A. I., and J. P. Lau (1973), A model for formation of transverse bars, *J. Geophys. Res.*, 78, 2656–2664.

Battjes, J. A. (1975), Modelling of turbulence in the surfzone, paper presented at Symposium on Modeling Techniques, Am. Soc. of Civ. Eng., San Francisco, Calif.

Bowen, A. J., and D. L. Inman (1969), Rip Currents: 2. Laboratory and field observations, *J. Geophys. Res.*, 74, 5479–5490.

Bruun, P. (1954), Coast erosion and the development of beach profiles, *U.S. Army Corps Eng. Tech. Memo 44*, Beach Erosion Board, Vicksburg, Miss.

Bühler, O., and T. E. Jacobson (2001), Wave-driven currents and vortex dynamics on barred beaches, *J. Fluid Mech.*, 449, 313–339.

Caballeria, M., G. Coco, A. Falques, and D. A. Huntley (2002), Self organization mechanisms for the formation of nearshore crescentic and transverse bars, *J. Fluid Mech.*, 465, 379–410.

Christensen, E., R. Deigaard, and J. Fresoe (1994), Sea bed stability on a long straight coast, in *Coastal Engineering 1994: Proceedings of the Twenty-Fourth International Conference*, edited by B. L. Edge, pp. 1865–1879, Am. Soc. of Civ. Eng., Reston, Va.

Clos-Arceduc, A. (1962), Effects de la reflexion sur un obstacle d'une houle de longuer d'onde 1, *Photo Interpretation*, 1, 1–10.

Dalrymple, R. A. (1975), A mechanism for rip current generation on the open coast, *J. Geophys. Res.*, 50, 3485–3487.

Damgaard, J., N. Dodd, L. Hall, and T. Chesher (2002), Morphodynamic modelling of rip channel growth, *Coastal Eng.*, 45, 199–221.

Dean, R. G. (1977), Equilibrium beach profiles: US Atlantic and Gulf Coasts, *Univ. of Del. Rep. 12*, Dep. of Civ. Eng., Ocean Eng., Newark, N. J.

Deigaard, R., N. Dronen, J. Fredsoe, J. H. Jensen, and M. P. Jorgensen (1999), A morphological stability analysis for a long straight barred coast, *Coastal Eng.*, 36, 171–195.

Falques, A., A. Montoto, and V. Iranzo (1996), Bed-flow instability of the longshore current, *Cont. Shelf Res.*, 16, 1927–1964.

Falques, A., G. Coco, and D. A. Huntley (2000), A mechanism for the generation of wave-driven rhythmic patterns in the surf zone, *J. Geophys. Res.*, 105, 24,701–24,087.

Fowler, R. E., and R. A. Dalrymple (1990), Wave group forced nearshore circulation, *Coastal Engineering Conference 1990: Proceedings of the International Conference*, edited by B. L. Edge, pp. 729–742, Am. Soc. of Civ. Eng., Reston, Va.

Galappatti, R. (1983), A depth integrated model for suspended transport, *Delft Univ. Rep. 83-7*, Dep. of Civ. Eng., Delft Univ. of Technol., Delft, Netherlands.

Herbers, T. H. C., S. Elgar, and R. T. Guza (1995), Generation and propagation of infragravity waves, *J. of Geophys. Res.*, 100, 24,863–24,872.

Hino, M. (1974), Theory on the formation of rip-current and cuspidal coast, *Coastal Engineering 1974*, pp. 901–191, Am. Soc. of Civ. Eng., Reston, Va.

Holman, R. A., and A. J. Bowen (1982), Bars, bumps and holes: Models for the generation of complex beach topography, *J. Geophys. Res.*, 87, 457–468.

Holthuijsen, L. H., N. Booij, and T. H. C. Herbers (1989), A prediction model for stationary short-crested waves in shallow water with ambient currents, *Coastal Eng.*, 13, 23–54.

Hom-ma, and C. Sonu (1963), Rhythmic pattern of longshore bars related to sediment characteristics, in *Proceedings of the 8th International Conference on Coastal Engineering*, pp. 248–278, Reston, Va.

Janssen, C. M., W. N. Hassan, R. v. d. Wal and J. S. Ribberink (1998), Grain-size influence on sand-transport mechanisms, in *Coastal Dynamics '97: Conference Proceedings of the Third Coastal Dynamics Conference held in Plymouth, U.K., June 1997*, edited by E. B. Thornton, pp. 58–67., Am. Soc. of Civ. Eng., Reston, Va.

Kennedy, J. F. (1963), The mechanics of dunes and antidunes in erodible-bed channels, *J. Fluid. Mech.*, 16, 521–544.

Klopman, G. (1995), Active wave absorption, *WL|Delft Hydraul. Rep. H1222*, Delft, Netherlands.

Komar, P. D. (1976), *Beach Processes and Sedimentation*, 429 pp., Prentice-Hall, Old Tappan, N. J.

Kuik, A. J., G. P. van Vledder, and L. H. Holthuijzen (1990), A method for the routine analysis of pitch-and-roll buoy data, *J. Phys. Oceanogr.*, 18, 1020–1034.

Lippmann, T. C., and R. A. Holman (1990), The spatial and temporal variability of sand bar morphology, *J. Geophys. Res.*, 95, 11,575–11,590.

Longuet-Higgins, M. S., and R. W. Stewart (1964), Radiation stress in water waves, a physical discussion with applications, *Deep Sea Res.*, 11, 529–563.

MacMahan, J., E. B. Thornton, T. Stanton, A. J. H. M. Reniers, and R. Dean (2003), RIPEX: Rip-current pulsation measurements, *Coastal Engineering 2002: Solving Coastal Conundrums*, edited by J. McKee Smith, pp. 736–746, World Sci., River Edge, N. J.

Nairn, R. B., J. A. Roelvink, and H. N. Southgate (1990), Transition zone width and implications for modelling surfzone hydrodynamics, in *Coastal Engineering Conference, 1990: Proceedings of the International Conference*, edited by B. L. Edge, pp. 68–81, Am. Soc. of Civ. Eng., Reston, Va.

Oltman-Shay, J., P. A. Howd, and W. A. Birkemeier (1989), Shear instabilities of the mean longshore current: 2. Field observations, *J. Geophys. Res.*, 94, 18,031–18,042.

Peregrine, D. H. (1998), Surf zone currents, *Theor. Comput. Fluid Dyn.*, 10, 295–309.

Phillips, O. M. (1977), *The Dynamics of the Upper Ocean*, 2nd ed., 336 pp., Cambridge Univ. Press, New York.

Ranasinghe, R., G. Symonds, and R. A. Holman (1999), Quantitative characterization of rip-dynamics via video imaging, in *Proceedings of Coastal Sediments '99*, pp. 987–1002, Am. Soc. of Civ. Eng., Reston, Va.

Reniers, A. J. H. M., J. A. Roelvink, and A. R. van Dongeren (2000), Morphodynamic response to wave group forcing, in *Coastal Engineering 2000: Conference Proceedings*, edited by B. L. Edge, pp. 3218–3228, Am. Soc. of Civ. Eng., Reston, Va.

Reniers, A. J. H. M., G. Symonds, and E. B. Thornton (2001), Modelling of rip currents during RDEX, in *Coastal Dynamics 2001*, edited by H. Hanson, pp. 493–499, Am. Soc. of Civ. Eng., Reston, Va.

Reniers, A. J. H. M., J. MacMahan, E. B. Thornton, and T. Stanton (2002a), RIPEX: Rip-current pulsation modeling, *Proceedings of the 28th International Conference on Coastal Engineering*, pp. 727–735, Am. Soc. of Civ. Eng., Reston, Va.

Reniers, A. J. H. M., A. R. Van Dongeren, J. A. Battjes, and E. B. Thornton (2002b), Linear modelling of infragravity waves during Delilah, *J. Geophys. Res.*, 107(C10), 3137, doi:10.1029/2001JC001083.

Ribas, F., A. Falqus, and A. Montoto (2003), Nearshore oblique sand bars, *J. Geophys. Res.*, 108(C4), 3119, doi:10.1029/2001JC000985.

Ribberink, J. S., and Z. Chen (1993), Sediment transport of fine sand in asymmetric oscillatory flow, *WL|Delft Hydraul. Rep. H840, Part VII*, Delft, Netherlands.

Rienecker, M. M., and J. D. Fenton (1981), A Fourier approximation method for steady water waves, *J. Fluid. Mech.*, 104, 119–137.

Roelvink, J. A., and M. J. F. Stive (1989), Bar generating cross-shore flow mechanisms on a beach, *J. Geophys. Res.*, 94, 4785–4800.

Roelvink, J. A. (1993a), Dissipation in random wave groups incident on a beach, *Coastal Eng.*, 19, 127–150.

Roelvink, J. A. (1993b), Surf beat and its effect on cross-shore profiles, Ph.D. thesis, 150 pp., Delft Univ. of Technol., Delft, Netherlands.

Roelvink, J. A., T. J. G. P. Meijer, K. Houwman, R. Bakker, and R. Spanhoff (1995), Field validation and application of a coastal profile model, in *Coastal Dynamics '95*, edited by R. b. Zeidler and W. R. Dally, pp. 818–828, Am. Soc. of Civ. Eng., Reston, Va.

Ryrie, S. C. (1983), Longshore motion due to an obliquely incident wave group, *J. Fluid Mech.*, 137, 273–284.

Schäffer, H. A. (1994), Edge waves forced by short-wave groups, *J. Fluid Mech.*, 259, 125–148.

Soulsby, R. L. (1997), *Dynamics of Marine Sands*, Thomas Telford, London.

Soulsby, R. L., L. Hamm, G. Klopman, D. Myrhaug, R. R. Simons, and G. P. Thomas (1993), Wave-current interaction within and outside the bottom boundary layer, *Coastal Eng.*, *21*, 41–69.

Stelling, G. S. (1984), On the construction of computational methods for shallow water flow problems, *Rijkswaterstaat Commun. 35*, The Hague, Netherlands.

Stive, M. J. F., and H. J. de Vriend (1994), Shear stresses and mean flow in shoaling and breaking waves, in *Proceedings of the Twenty-Fourth International Conference*, edited by B. L. Edge, pp. 594–608, Am. Soc. of Civ. Eng., Reston, Va.

Stokes, G. G. (1847), On the theory of oscillatory waves, *Trans. Cambridge Philos. Soc.*, *8*, 441–455.

Symonds, G., and R. Ranasinghe (2000), On the formation of rip currents on a plane beach, in *Coastal Engineering 2000: Conference Proceedings*, edited by B. L. Edge, pp. 3218–3228, Am. Soc. of Civ. Eng., Reston, Va.

Symonds, G., D. A. Huntley, and A. J. Bowen (1982), Two dimensional surf-beat: Long wave generation by a time-varying break point, *J. Geophys. Res.*, *87*, 492–498.

Tang, E. C.-S., and R. A. Dalrymple (1989), Nearshore circulation: Rip currents and wave groups, *Nearshore Sediment Transport*, edited by R. J. Seymour, Plenum, New York.

Thornton, E. B., and C. S. Kim (1993), Longshore current and wave height modulation at tidal frequency inside the surfzone, *J. Geophys. Res.*, *98*, 16,509–16,519.

Van Dongeren, A., A. Reniers, J. Battjes, and I. Svendsen (2003), Numerical modeling of infragravity wave response during DELILAH, *J. Geophys. Res.*, *108*(C9), 3288, doi:10.1029/2002JC001332.

Van Enckevort, I. M. J., and B. G. Ruessink (2001), Effect of hydrodynamics and bathymetry on video estimates of nearshore sandbar position, *J. Geophys. Res.*, *106*, 16,969–16,980.

Van Rijn, L. C. (1993), *Principles of Sediment Transport in Rivers, Estuaries and Coastal Seas*, Aqua, Amsterdam.

Verboom, G. K., and A. Slob (1984), Weakly-reflective boundary conditions for two-dimensional water flow problems, in *Finite Elements in Water Resources: Proceedings of the 5th International Conference, Burlington, Vermont, USA, June 1984*, edited by J. P. Laible et al., Springer, New York.

Wijnberg, K. M., and J. H. J. Terwindt (1995), Quantification of decadal morphological behavior of the central Dutch coast, *Mar. Geol.*, *126*, 301–330.

Wright, L. D., and A. D. Short (1984), Morphodynamic variability of surfzones and beaches: A synthesis, *Mar. Geol.*, *56*, 93–118.

Wright, L. D., J. Chappell, B. G. Thom, M. P. Bradshaw, and P. Cowell (1979), Morphodynamics of reflective and dissipative beaches and inshore systems: Southeastern Australia, *Mar. Geol.*, *32*, 105–140.

Yu, J., and D. N. Slinn (2003), Effects of wave-current interaction on rip currents, *J. Geophys. Res.*, *108*(C3), 3088, doi:10.1029/2001JC001105.

————————————

A. J. H. M. Reniers, Faculty of Civil Engineering and Geosciences, Delft University of Technology, Stevinweg 1, 2628 CN, Delft, Netherlands. (a.j.h.m.reniers@citg.tudelft.nl)

J. A. Roelvink, WL|Delft Hydraulics, P.O. Box 177, 2600 MH, Delft, Netherlands.

E. B. Thornton, Oceanography Department, Naval Postgraduate School, Monterey, CA 93943, USA